High-Temperature Materials

SCIEPublish

Review

Development of Novel 20Cr Ferritic Stainless Steels via Nanoscale G-Phase Dispersion Strengthening: A Brief Review

Mujin Yang [1], Daobin Zhang [1], Dingding Zhu [1], Bo Du [1], Minglin He [1], Jiang Yi [1,*], Zhifu Yao [2,*], Shuai Wang [1,3], Cuiping Wang [4,5] and Xingjun Liu [6,7,*]

[1] Department of Mechanical and Energy Engineering, Southern University of Science and Technology, 1088 Xueyuan Blvd, Shenzhen 518055, China; yangmj@sustech.edu.cn (M.Y.); 12232344@mail.sustech.edu.cn (D.Z.); zhudd@sustech.edu.cn (D.Z.); dub3@sustech.edu.cn (B.D.); heml@sustech.edu.cn (M.H.); wangs@sustech.edu.cn (S.W.)
[2] Sino-German College of Intelligent Manufacturing, Shenzhen Technology University, Shenzhen 518118, China
[3] College of Energy and Engineering, Zhejiang University, Hangzhou 310027, China
[4] Fujian Key Laboratory of Surface and Interface Engineering for High Performance Materials, School of Materials Science, Xiamen University, Xiamen 361005, China; wangcp@xmu.edu.cn (C.W.)
[5] Xiamen Key Laboratory of High Performance Metals and Materials, School of Materials Science, Xiamen University, Xiamen 361005, China
[6] School of Metallurgy and Energy Engineering, Kunming University of Science and Technology, Kunming 650093, China
[7] Department of Materials Science and Engineering, Harbin Institute of Technology, Shenzhen 518055, China

* Corresponding author. E-mail: yij@sustech.edu.cn (J.Y.); yaozhifu@sztu.edu.cn (Z.Y.); xjliu@hit.edu.cn (X.L.)

Received: 3 February 2026; Revised: 9 April 2026; Accepted: 18 June 2026; Available online: 29 June 2026

ABSTRACT: Extensive investigations have revealed the precipitation of nanometer-scale silicides, identified as G-phase, within the ferritic matrix of duplex stainless steels during prolonged thermal aging. These silicides typically exhibit a well-defined coherent orientation relationship with the ferrite matrix, specifically ($100_G//100_F$, $110_G//110_F$, $111_G//111_F$). Consequently, the authors and their research team proposed a novel concept in 2015: utilizing the G-phase as a primary strengthening phase. It was proposed that through strategic alloy design, these silicides—ordinarily considered deleterious in duplex stainless steels—could be used to develop a new generation of dispersion-strengthened ferritic stainless steels. This approach aims to significantly enhance the yield strength of the alloy while maintaining excellent tensile ductility. Over the past decade, the authors and their research team have focused on nanoscale G-phase dispersion-strengthened ferritic stainless steels. By combining first-principles calculations with thermodynamic database-driven alloy design, a series of new ferritic stainless steel systems based on G-phase strengthening has been developed. These efforts have yielded extensive fundamental results regarding the compositional control, microstructural design, and mechanical properties of silicide-strengthened 20Cr ferritic stainless steels. Based on a comprehensive review of the existing literature, this paper further summarizes the compositional design criteria and microstructural control strategies for G-phase strengthened steels. It is hoped that this work will encourage further fundamental research and industrial applications in this field.

Keywords: Silicide G-phase; Ferritic stainless steels; Precipitation strengthening; Strength-ductility synergy

1. Introduction

The relentless demand for advanced structural materials with superior mechanical properties, particularly high strength and excellent ductility, continues to drive innovation in metallurgy. Overcoming the inherent strength-ductility trade-off remains a central challenge, leading to the exploration of diverse strengthening mechanisms. Beyond traditional solid solution and work hardening, strategies such as grain refinement, twinning-induced plasticity (TWIP), transformation-induced plasticity (TRIP), and, critically, nanoprecipitation strengthening have emerged as highly effective routes for developing next-generation high-performance steels. Recent breakthroughs, exemplified by ultra-high-strength maraging steels strengthened by B2-NiAl particles [1], 'super steels' with unprecedented yield strength achieved through high dislocation density [2], sustainable ultra-high-strength maraging steels utilizing α-Mn nanoprecipitation [3], and bulk ultrafine-grained TWIP steels with rapid Cu-nanoprecipitation [4], underscore the transformative potential of controlling microstructure at the nanoscale. These examples highlight that identifying and optimizing effective strengthening phases compatible with the matrix is paramount for achieving an optimal combination of strength and toughness.

Within this landscape of advanced strengthening mechanisms, the silicide G-phase presents a unique and intriguing case. Traditionally regarded as a detrimental precipitate in aged duplex stainless steels due to its complex face-centered cubic (FCC) structure (space group Fm-3m (225), a = 11.257 Å, 116 atoms per unit cell) [5,6], its precipitation at grain boundaries has long been associated with embrittlement. Consequently, research on its strengthening potential was historically limited. However, a paradigm shift occurred with the work of Hutchinson et al. [7] in 2017, who demonstrated the efficacy of G-phase silicides as strengthening agents in maraging steels. By achieving an exceptionally high number density ($10^{25}/m^3$) of G-phase precipitates, they developed alloys with yield strengths up to 2 GPa, revealing a dislocation-shearing mechanism and a significant aging response. The following sections provide a comprehensive review of the evolution of research on G-phase in steels and other relevant alloy systems.

In various austenitic alloys, the precipitation behavior of the G-phase during long-term thermal aging and high-temperature service is a critical factor governing the microstructural stability and mechanical properties. In high-Si austenitic stainless steels, Si has been shown to promote the formation of a multiphase structure composed of G-phase and ferrite, in which G-phase precipitates at grain boundaries prior to ferrite formation, ultimately leading to a dramatic decrease in impact toughness [8]. Similarly, in 30Cr2Ni4MoV steel aged at 350–600 °C, G-phase (identified as $Ni_{16}Mn_6Si_7$) predominantly forms at grain boundaries and triple junctions in conjunction with $M_{23}C_6$ carbides [9]. Long-term service exposure also facilitates G-phase precipitation; for instance, in Ti-stabilized austenitic stainless steel after 207,000 h of service at 540 °C, G-phase was observed to precipitate adjacent to $M_{23}C_6$ carbides [10]. In heat-resistant cast austenitic steels, such as 20Cr32Ni1Nb and HP series alloys, the formation of Ni-Nb silicides (G-phase) at interdendritic boundaries or at the expense of primary MC carbides during prolonged high-temperature service has been identified as a key mechanism of microstructural degradation and embrittlement [11–13].

Under irradiation environments, such as those encountered in nuclear reactors, the formation of G-phase is significantly accelerated by radiation-induced segregation and enhanced diffusion rates. In austenitic stainless steels like AISI316, neutron irradiation promotes the unexpected precipitation of G-phase at lower temperatures due to the segregation of Ni and Si [14,15]. Heavy ion and proton irradiations of cast austenitic stainless steels (CASS) and weld metals further demonstrate that G-phase readily precipitates within the ferrite matrix or δ-ferrite [13,16,17]. The kinetics of G-phase precipitation in these duplex steels are highly dependent on alloying elements; specifically, additions of Mo and Mn promote G-phase precipitation, while Ni accelerates the concurrent spinodal decomposition kinetics [18]. Advanced characterization reveals that the segregation of Ni and Si at decomposed interfaces contributes to G-phase nucleation, and irradiation can even induce an unusual inverse coarsening behavior in these precipitates [17].

Conversely, the strategic manipulation of G-phase precipitation offers a viable pathway for achieving ultra-high strength in advanced steels. In a medium-Mn stainless steel, room-temperature deformation induced martensitic transformation, and subsequent aging at 400 °C led to the formation of ultrafine (2–3 nm) G-phase precipitates containing Cu-rich clusters [19]. This unique microstructure, combining strain-induced martensite and nanoscale G-phase, successfully unlocked ultra-high flow stress and hardness (reaching ~2.2 GPa) in the steel [19]. In summary, while coarse G-phase precipitation during long-term thermal aging or irradiation generally degrades the ductility and toughness of stainless steels [8–10,14,15], its controlled nucleation and growth—especially in the form of nanoscale particles—presents a powerful avenue for strengthening advanced high-performance steels [19]. These findings provide crucial guidelines for the microstructural design and life assessment of steel components in demanding engineering applications.

In martensitic steels, the G-phase is established as an FCC silicide with a lattice parameter $\boldsymbol{a}_G \approx 4\boldsymbol{a}_{bcc}$, providing a near cube-on-cube orientation relationship with the martensitic matrix [20,21]. Its archetypal stoichiometry is $Ti_6Si_7Ni_{16}$, though it tolerates partial Fe/Mn substitution in engineering alloys [20,22]. Crucially, its formation is Si-gated: in Ti-bearing but Si-poor systems, the precipitation track collapses to NiAl(B2)/η-Ni_3Ti with no G-phase [23,24], while Ti-lean/Si-lean compositions do not open the G-channel at all [7].

In the Cr-containing maraging lineage, adding Ti + sufficient Si shifts the early ageing path (475–525 °C) from a single NiAl lineage to a co-segregated Ni–Al–Ti–Si(±Cu) precursor that partitions: Ni/Al/(Cu) consolidate toward B2-type domains, while Ti and Si condense into near-spherical G-phase cores that reject Cu/Al, often retaining an Al/Si/Cu interfacial shell [23,25]. Bulk-sensitive SANS/EFTEM quantifies the dominant G-like dispersion as small, Ni–Ti–Si-enriched spheres with radii growing from ≤1 nm to 1.5–2 nm, volume fractions 5–8%, and number densities 10^{18}–10^{19} cm^{-3} [26,27]. The A-ratio (magnetic/nuclear SANS) is substantially closer to the calculated value for $Ti_6Si_7Ni_{16}$ than for Ni_3Ti, supporting a G-phase assignment while warning that G + η coexistence can be obscured by single-phase fitting [26,28]. Mechanically, the combined early volume fraction of G + η can compress interparticle spacing to 4–5 nm, correlating with a transient intergranular/cleavage-dominant fracture window before overaging restores ductility via Orowan bypass and reverted austenite [29].

A distinct, service-temperature analogue appears in 17-4 PH martensite: after long-term aging at 400 °C, the matrix undergoes spinodal-type decomposition, and fine G-phase particles ($Ni_{55}Si_{25}Fe_{20}$, with Mn) appear in intimate contact with ε-Cu precipitates [22]. Here, the dominant embrittlement driver is attributed to the Cr-rich α′ spinodal, not G-phase *per se*. By contrast, Sun et al. [7] moved G-phase to the design centre: in lean, ultra-low-C Fe–Si–Ti–Mn–Ni(–Cr) lath martensites, they maximized G-phase's Number denity ($N \sim 10^{24}$–10^{25} m^{-3}), volume fraction (V_f~4–5.6%) and radius radii (R~1.5–2.6 nm). Relating strength (~1.68–1.71 GPa) to a shear-cut/coherency picture, they reported back-calculated G-phase/matrix interfacial energies in the γ~0.02–0.10 J/m^2 range, demonstrating that $Ti_6Si_7Ni_{16}$ can serve as the primary nanospherical strengthener in "lean maraging" metallurgy.

In duplex stainless steels, the G-phase is a nanoscale, face-centered-cubic (FCC) intermetallic silicide that precipitates exclusively within the ferrite (δ/α) phase during long-term exposure to the 280–475 °C temperature regime. It is universally characterized by space group Fm-3m, a lattice parameter $a_G \approx 1.09$–1.15 nm (approximately four times that of the bcc ferrite matrix), and a dominant cube-on-cube orientation relationship: $(001)_G \| (001)_\alpha$, and $[100]_G \| [100]_\alpha$ [6,30–32]. While its ideal stoichiometry is often approximated as $(Ni,Fe)_{16}(Mn,Cr)_6Si_7$, the G-phase in real alloys is chemically heterogeneous: Ni, Si, Mn, and Mo (when present) are enriched, whereas Fe and Cr are progressively expelled during coarsening [32–35]. In lean grades, Cu can also participate, leading to core-shell structures [36,37].

G-phase formation is inseparably coupled to ferrite spinodal decomposition (α → Cr-rich α′ + Fe-rich α). G-forming elements (Ni, Si, Mn, Mo, Cu) are rejected from the growing α′ domains and accumulate along the interconnected α/α′ interfacial network. Once a critical local concentration and cluster size are

reached, these solute-enriched zones transform into crystalline G-phase via only sub-interatomic-scale atomic displacements, without long-range diffusional reconstruction [6,33,38,39]. Dislocations and α/γ phase boundaries act as preferred nucleation corridors, accelerating both spinodal kinetics and G-phase precipitation [31,40].

A critical spatial heterogeneity has been revealed by combined TEM and atom probe tomography (APT): the number density of G-phase precipitates is not uniform across the ferrite. In CF3M cast duplex stainless steel aged at 673 K, the number density is strongly suppressed within ≈ 4 μm of the α/γ interface, reaching a saturated value of ~1.8×10^{23} m^{-3} only in the ferrite interior [31]. This "near-boundary dead zone" arises because Mo, Si, and C segregate to the interface, depleting the adjacent ferrite of G-forming elements. Such spatial gating explains the scatter in APT-derived number densities and underscores that "average ferrite" values must be interpreted with reference to sampling location.

The kinetics of G-phase precipitation and spinodal decomposition follow a power-law dependence, $R(t) \propto t^n$, but with distinct time exponents. In CF3M aged at 623–723 K, the exponent for G-phase coarsening (n_G = 0.086–0.244) consistently exceeds that for spinodal wavelength evolution (n_{spin} = 0.078–0.097), and both increase with temperature [32]. The activation energy governing Cr concentration variations is Q ≈ 272 kJ/mol, consistent with Cr/Fe diffusion in α-Fe, confirming that the overall microstructural evolution is diffusion-controlled [32]. At advanced aging (e.g., 673 K/5000 h), G-phase particles are fully crystallized and detectable by TEM dark-field imaging; at earlier stages (e.g., 2000 h), a population of smaller, bcc-structured Ni–Si–Mn–Mo clusters exists that are APT-visible but TEM-invisible, representing pre-G precursors [31].

Alloy composition governs the G-phase precipitation pathway. In standard, Mo-bearing grades such as 2205 (ferrite Ni ≈ 4 at%), G-phase nucleates with simultaneous enrichment of Ni, Cu, and Si, showing no core-shell structure, and achieves a number density approximately one order of magnitude higher than in lean grades [36]. In contrast, lean-grade 2101 (very low Ni, high Mn/Si, small Cu) follows a three-stage evolution: (I) Cu-rich clusters form first at α/α′ interfaces; (II) Ni–Mn–Si envelop these clusters, creating a Cu-core/Ni–Mn–Si-shell architecture; (III) Ostwald ripening reduces the number density while coarsening the survivors [36,37]. Alloy 2003, with even lower G-former content, exhibits negligible G-type clustering altogether [37]. Importantly, 2101 also shows Mn and Si segregation into the Cr-rich α′ phase, a feature absent in 2205 and 2003, which accelerates spinodal decomposition and modifies the α/α′ lattice mismatch [37]. These findings demonstrate that Cr_{eq}/Ni_{eq} heuristics alone are insufficient to predict G-phase susceptibility; the individual roles of Mn, Cu, and residual Ni must be considered.

Functionally, the G-phase degrades mechanical integrity through dual pathways. Mechanistically, it acts as a potent, nanoscale obstacle to dislocation motion. Quantitative Ashby–Orowan hardening estimates show that the higher G-phase number density in 2205 explains its faster ferrite hardening, despite its spinodal amplitude being smaller than that in 2101 [36]. Corrosively, the G/α interface introduces localized strain fields and compositional discontinuities that serve as preferential initiation sites for pitting and selective dissolution in chloride-containing environments [30,41]. The embrittlement risk is therefore gated both spatially (by the α/γ boundary halo) and chemically (by the available G-former budget in ferrite).

Finally, in copper alloys, recent studies have fundamentally reshaped the understanding of the G-phase ($A_{16}M_6Si_7$), shifting its perception from a detrimental grain boundary embrittler to a powerful strengthening agent [42–44]. Characterized by a complex face-centered cubic structure, this intermetallic silicide exhibits a strong tendency for heterogeneous nucleation at grain boundaries. Research demonstrates that its morphology and distribution can be precisely engineered through compositional design and processing control. For instance, increasing Si content promotes the transformation of grain boundary phases into thin, film-like structures in Mn-containing alloys [44], while micro-alloying with elements like Sr or P effectively refines the particles or alters their growth anisotropy via adsorption-poisoning mechanisms [45,46], leading to more spherical or cubic geometries. The strategic utilization of the G-phase unlocks exceptional mechanical and functional properties. Its significant hardness disparity with the Cu matrix induces

substantial Heterogeneous Deformation Induced (HDI) strengthening, successfully decoupling the traditional trade-off between strength and ductility [42]. This is evidenced by the achievement of ultra-high tensile strengths exceeding 1.3 GPa while retaining elongations of ~6% in Cu–Ni–Mn–Si systems. Furthermore, controlled G-phase precipitation enhances wear resistance by up to 80% [45] and stabilizes grain boundaries against migration, thereby providing excellent high-temperature microstructural stability [43].

These findings offer clear guidelines for next-generation Cu-based alloy design. By actively incorporating G-phase formers such as Ti, Zr, or Mn, and employing tailored thermo-mechanical processing, the G-phase can be optimized as a potent grain refiner and load-bearing phase [44,46]. This approach not only elevates the mechanical performance of high-strength copper alloys but also leverages the G-phase's ability to "capture" reactive elements like Zr, mitigating oxidation losses during atmospheric melting and reducing manufacturing costs [43].

Building upon the above foundational understanding and drawing from extensive experience in alloy design, our research team proposed, in 2015, a novel concept: intentionally harnessing the G-phase as a primary strengthening precipitate in iron-based alloys [47–50]. The audacious goal was to transform this conventionally detrimental phase into a beneficial one, paving the way for a new class of dispersion-strengthened ferritic stainless steels, termed 'G-phase steels'. This innovative approach aims to significantly enhance the strength of ferritic alloys while maintaining excellent tensile ductility.

This paper provides a comprehensive and critically evaluated review of the recent advancements in G-phase strengthened ferritic stainless steels. We delve into the intricate aspects of alloy design, microstructural evolution, and mechanical properties. Crucially, we aim to contextualize G-phase strengthening within the broader spectrum of advanced strengthening mechanisms, including oxide dispersion strengthened (ODS) steels, maraging steels, and other nanoprecipitate-hardened systems. By comparing and contrasting G-phase steels with these established and emerging material classes, we seek to highlight the unique advantages, inherent challenges, and future research directions for G-phase strengthened materials, moving beyond a purely descriptive account to offer a balanced and critical perspective. We also propose refined design criteria and control methods to facilitate their future development and industrial application.

2. Alloy Design Strategies

The design of G-phase strengthened steels is a multi-scale and multi-objective optimization process. Its core lies in the precise selection of promising ternary G-phase systems through theoretical calculations, which then guides the alloy composition design and experimental validation.

2.1. Typical Ternary Phase Diagrams Containing G-Phase

Studies on the Fe–Zr–Si ternary system have reported the existence of the G-phase as $Fe_{16}Zr_6Si_7$ [51,52]. Its key features in the isothermal section at 1000 °C are as follows (Figure 1): First, the solubility range of the G-phase on the Fe-rich side is parallel to the Fe–Si binary side. This suggests that Fe and Si atoms have a degree of mutual substitution within the G-phase lattice, leading to the formation of non-stoichiometric phases with compositional deviations. Secondly, the G-phase maintains phase equilibrium with multiple phases, including α-Fe (body-centered cubic, Im-3m). However, the solubility of Zr in α-Fe is extremely low (<1 at.%). This indicates that while the precipitation driving force for the $Fe_{16}Zr_6Si_7$-G phase in ferritic steels is high, its volume fraction remains limited. Other coexisting phases include Fe_2Zr (C15-type Laves phase, Fd-3m), a common Zr-rich intermetallic, as well as the τ_1 phase (FeZrSi, orthorhombic, Pnma) and τ_8 phase (Fe_4Si_2Zr, tetragonal, P42/mmm). These intermetallic compounds increase the complexity of the phase diagram. In addition to $Fe_{16}Zr_6Si_7$, other G-phase variants such as $Fe_{16}Hf_6Si_7$, $Fe_{16}Nb_6Si_7$, and

$Fe_{16}Ta_6Si_7$ have been reported. However, detailed phase diagram data for these systems are not yet available, indicating that further experimental characterization of Fe-based G-phase systems is still required.

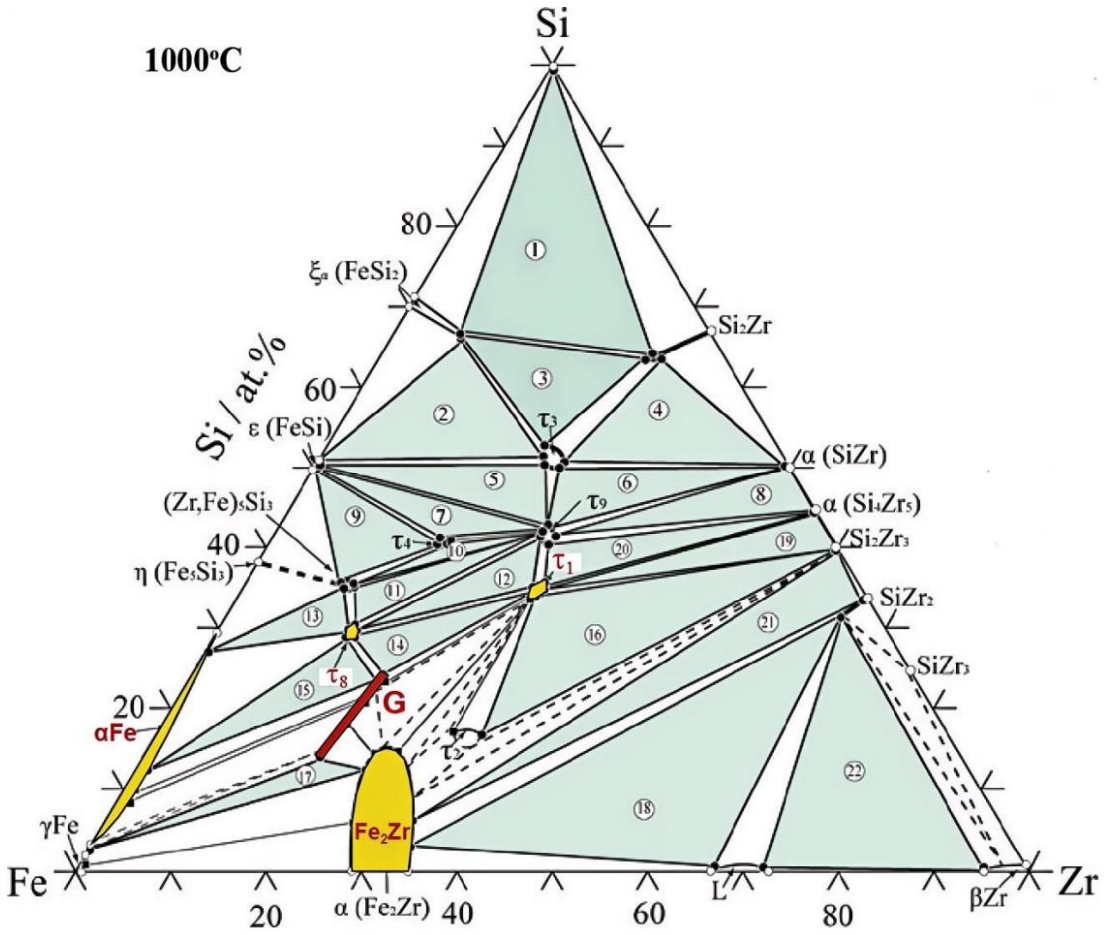

Figure 1. Isothermal section of the Fe–Zr–Si ternary system containing G-phase at 1000 °C.

Similarly, research on the Ni–Ti–Si ternary system indicates that the G-phase exists as $Ni_{16}Ti_6Si_7$ [53]. The isothermal sections at 750 °C and 1100 °C are shown in Figure 2. A prominent feature of this system is that the solubility range of the G-phase expands significantly with increasing temperature. At 1100 °C, the G-phase region is wider than at 750 °C, indicating enhanced mutual solubility of elements at high temperatures. Furthermore, the G-phase maintains phase equilibrium with several binary and ternary phases, including the τ_1 phase (NiTiSi, orthorhombic, Pnma), τ_2 phase (Ni_3Ti_2Si, Laves phase, hexagonal, $P6_3/mmm$), τ_7 phase ($Ni_{49}Ti_{14}Si_{37}$, hP68), and Ni_3Ti ($P6_3/mmm$). Notably, the τ_1 phase shares the same space group and a similar chemical composition as the τ_1 phase (FeZrSi) in the Fe-based system, indicating cross-system structural similarity. Interestingly, the G-phase does not directly equilibrate with the γ-Ni solid solution (FCC). This differs from the Fe-based system, where the G-phase equilibrates with α-Fe, which likely affects the precipitation pathways and kinetics of the G-phase in Ni-based alloys.

The Co-based phase diagram [54] (Figure 3) exhibits high similarity to the Fe- and Ni-based systems. For instance, the τ_2 phase (Co_3Ti_2Si) is a Laves phase, analogous to the τ_2 phase (Ni_3Ti_2Si) in the Ni-based system, and the solubility behavior of the G-phase is consistent. This suggests that the G-phase follows universal formation rules across different matrices, likely stemming from its common crystal structure and bonding characteristics. The summary of ternary phase diagram data [49,51] (covering 17 ternary alloy systems) in Table 1 reveals clear trends in G-phase distribution. The Ni-based systems contain the highest number of G-phases, all of which are thermodynamically stable (e.g., in Ni–Ti–Si, Ni–Zr–Si, and Ni–Hf–Si). These phases readily form under equilibrium conditions due to strong interactions between Ni and the

X elements (Ti, Zr, Hf) or Si, which are characterized by a highly negative enthalpy of formation. In contrast, the Fe-based systems have the fewest G-phases, half of which are metastable (e.g., $Fe_{16}Nb_6Si_7$ and $Fe_{16}Ta_6Si_7$). This implies they may precipitate under non-equilibrium conditions (such as rapid cooling or aging) but could transform into other phases during long-term service. The Co-based systems fall between the Ni and Fe systems in terms of G-phase abundance and stability, with most being stable phases, though further experimental validation is still required for some systems.

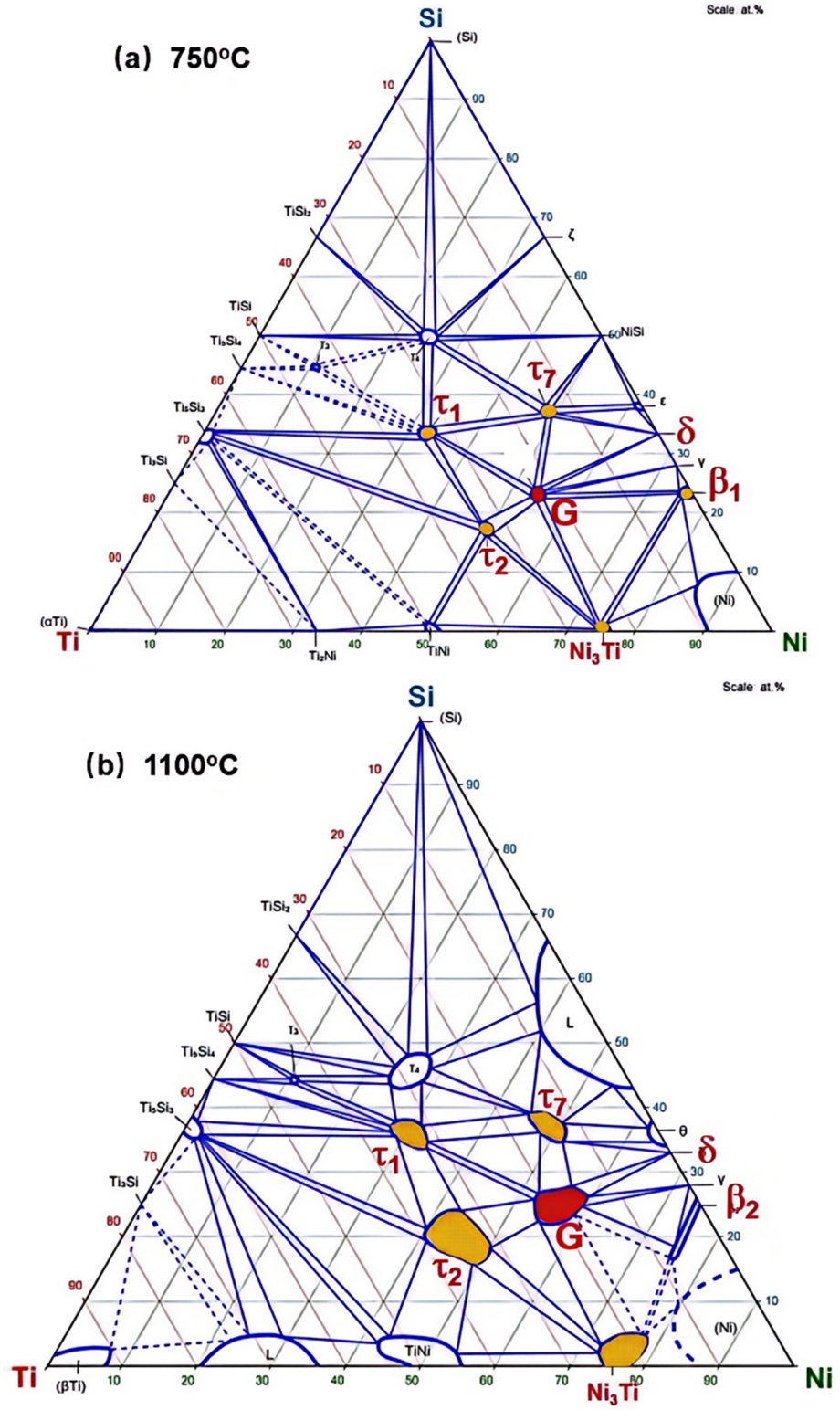

Figure 2. Isothermal sections of the Ni–Ti–Si ternary system containing G-phase at (**a**) 750 °C and (**b**) 1100 °C.

In summary, across all systems (Fe, Co, and Ni), the G-phase is located in the matrix-rich region. Its solubility range allows for compositional fluctuations, supporting its non-stoichiometric behavior. The G-phase maintains equilibrium with multiple ternary compounds (e.g., τ_1, τ_2) and binary intermetallic phases. This high complexity reflects that its formation is governed by multiple thermodynamic constraints. The consistency of the Pnma structure for the τ_1 phase in both Fe and Ni systems highlights the structural stability of transition-metal silicides across different matrices. The solubility of the G-phase is temperature-dependent. While this is most pronounced in the Ni system, a similar trend is anticipated for Fe and Co systems despite limited data. Crucially, the G-phase equilibrates with α-Fe in the Fe system but not with γ-Ni in the Ni system, which likely leads to different precipitation pathways. While the low solubility of Zr in the Fe system limits the G-phase volume fraction, the precipitation amount in Co and Ni systems can be optimized by adjusting Ti and Si contents. These stability and solubility characteristics directly determine the aging treatment window. For compositional optimization, preference should be given to X elements such as Ti, Zr, Hf, Nb, and Ta to ensure G-phase stability, with Si content adjusted (typically 2–4 at.%) to match the solubility range. To develop new G-phase strengthened steels, it is essential to expand phase diagram databases—particularly for Fe and Co systems—and combine them with first-principles calculations to predict the behavior of metastable phases. In conclusion, the thermodynamic study of G-phase in ternary systems provides the foundation for its application as a strengthening phase. While the Ni system is currently favored for its superior stability, the Fe and Co systems require further optimization to overcome metastability limitations.

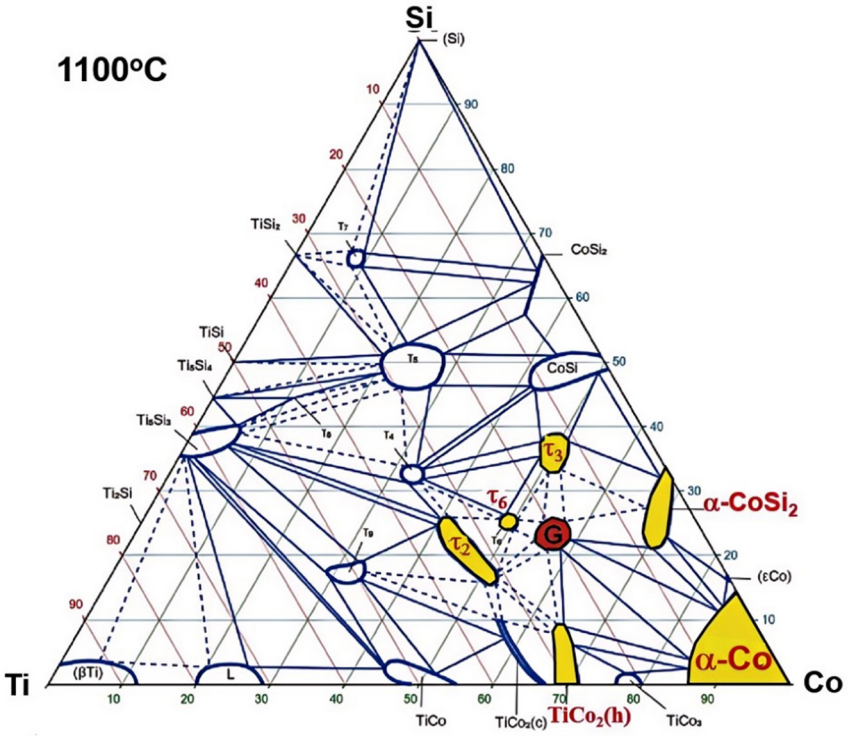

Figure 3. Isothermal section of the Co–Ti–Si ternary system containing G-phase at 1100 °C.

Table 1. Distribution of ternary G-phases in transition metal systems.

Transition Element A	Transition Element B											
	Group IV			Group V			Group VI			Group VII		
	Ti	Zr	Hf	V	Nb	Ta	Cr	Mo	W	Mn	Tc	Re
Fe	X	G	G	X	G *	G *	X	X	X	X	X	X
Co	G	G	G	X	G	G	X	X	X	X	X	X
Ni	G	G	G	G	G	G	G *	X	X	G	X	X

*: Ternary metastable G-phase. X: Absence of ternary G-phase.

2.2. First-Principles Calculations of G-Phase

Physical and chemical properties of silicide G-phases (see the crystal model in Figure 4) were predicted using Density Functional Theory (DFT) calculations coupled with the quasi-harmonic Debye model [50,55]. The screening criteria revolve around thermodynamic stability, lattice misfit, and intrinsic ductility, though specific parameters vary depending on the G-phase composition. The screening process is primarily based on three core principles: (a) Rapid Precipitation Principle: The formation enthalpy (ΔH) of the G-phase at the ground state (0 K) is calculated to evaluate its thermodynamic stability. A more negative formation enthalpy indicates a higher propensity for formation, a greater precipitation driving force, and a shorter incubation period. (b) Low Misfit Principle: The lattice misfit (δ) between the G-phase and the ferrite matrix (α-Fe) is critical for strengthening efficiency and ductility. By calculating the lattice constants of both phases and predicting their high-temperature thermal expansion behavior via the quasi-harmonic Debye model, the optimal aging temperature for achieving low or even zero misfit can be determined. (c) Intrinsic Ductility Principle: To prevent the secondary phases from inducing brittleness, the intrinsic ductility/brittleness of the G-phase is assessed. This is done by calculating the elastic constants (C_{11}, C_{12}, C_{44}) and deriving the Pugh's ratio (B/G) and Cauchy pressure (C_{12}-C_{44}). A value of B/G > 1.75 and a positive Cauchy pressure indicate that the material possesses good intrinsic ductility.

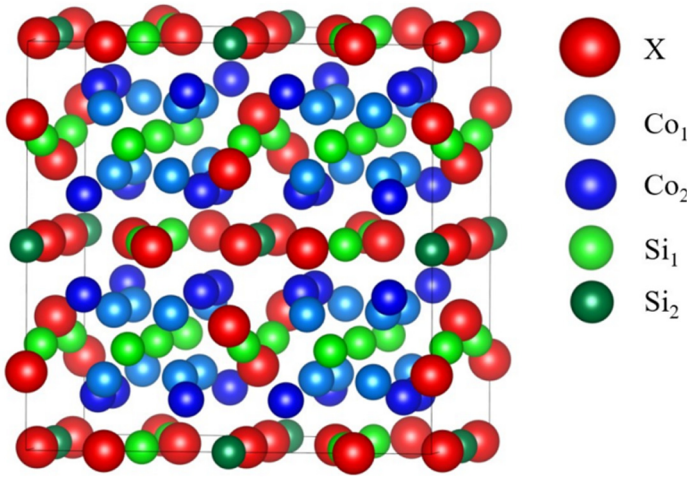

Figure 4. Crystal structure model of the ternary $Co_{16}X_6Si_7$-G phase.

Our first-principles calculations, as reported by Daniel and Wang et al. [55,56], demonstrated that all G-phases are stable at 0 K (ΔH < 0). The corresponding physical parameters of G-phases in different systems are listed in Table 2. However, Ni-based and Co-based G-phases (X = Zr, Hf, Ti, Nb, Ta) exhibit the highest stability (ΔH < −0.55 eV/atom), whereas Fe-based G-phases show slightly lower stability (ΔH < −0.40 eV/atom). Gibbs free energy (ΔG) analysis reveals that the entropy contribution at elevated temperatures affects relative stability; for instance, the stability rankings of $Ni_{16}Mn_6Si_7$-G and $Fe_{16}Re_6Si_7$-G phases shift near 900 K. Lattice misfit analysis indicates that Co-based and Fe-based G-phases can achieve low misfit (δ < 0.5%) or even zero misfit within the 850–950 K range (e.g., $Co_{16}Nb_6Si_7$-G at 870 K). In contrast, the aging temperature for Ni-based G-phases must be carefully tuned between 700–900 K to optimize the misfit. Low misfit effectively reduces the nucleation barrier, promoting dispersed precipitation. Furthermore, calculations of the Pugh's ratio (B/G) and Cauchy pressure suggest that most G-phases are intrinsically ductile (B/G > 1.75). However, Fe-based G-phases containing X = Hf, Zr, or V exhibit brittle behavior. Charge density difference analysis further clarifies that the strength of the Co–X bond dominates the elastic modulus, while the influence of the Si–X bond is relatively minor.

Table 2. Comparison of formation enthalpies, lattice misfits, key elastic properties, and high-temperature misfits of G-phases in different systems.

G-Phase System	Optimal X Element	Lattice Misfit δ (%)	Elastic Properties B/G > 1.75 Positive Cauchy Pressure	Temperature Range for δ ≈ 0
$Ni_{16}X_6Si_7$	Zr, Hf, Ti, Nb, Ta (ΔH < −0.55)	−5.13–0	Intrinsic ductility B/G ~1.8–2.0	700–900 K
$Co_{16}X_6Si_7$	Zr, Hf, Ti, Nb, Ta (ΔH < −0.55)	−2.32–0.15	Intrinsic ductility B/G ~1.8–2.2	850–950 K
$Fe_{16}X_6Si_7$	Zr, Hf, Ti, Nb, Ta (ΔH < −0.40)	−2.50–0.60	Intrinsic ductility excluding X = Hf, Zr, V	750–950 K

2.3. Compositional Selection for G-Phase Strengthened Steels

Based on the survey of ternary phase diagrams and the first-principles calculations of physicochemical properties, the research team utilized commercial thermodynamic databases for Fe-based alloys to design the compositions and heat treatment processes. The compositional design of G-phase strengthened steels is a multi-objective optimization process that balances thermodynamic stability, precipitation kinetics, and strengthening efficiency. The core strategies are as follows: (1) Matrix Selection: Selecting a corrosion-resistant ferritic matrix, such as Fe-20Cr (wt.%). (2) Solute Balancing: Ensuring sufficient concentrations of Ni, Si, and X (solute elements) to promote the formation of the G-phase. (3) Optimization of Forming Elements: Carefully selecting and pairing G-phase forming elements (e.g., Ti alone, or a Mn/Zr combination) and optimizing their contents through thermodynamic calculations.

This approach to compositional design, focusing on the precise control of solute elements for targeted nanoprecipitation, shares commonalities with other precipitation-strengthened systems like maraging steels (e.g., controlling Ni, Al, Ti for B2-NiAl or Ni_3Ti precipitation) and certain high-strength low-alloy (HSLA) steels (e.g., optimizing Nb, V, Ti for carbide/nitride precipitation). However, the compositional design of G-phase strengthened steels faces inherent limitations, particularly concerning cost and alloy complexity. Key alloying elements such as Ni and Ti, while crucial for G-phase formation and stability, are relatively expensive, which can significantly impact the overall material cost and limit widespread industrial adoption. This necessitates a strategic shift towards developing low-Ni or even Ni-free G-phase strengthened alloys, as further elaborated in the 'Future Perspectives' section. Moreover, the multi-component nature of these alloys, involving precise control over Ni, Si, and various X-elements, introduces considerable complexity in terms of phase control. Achieving the desired G-phase volume fraction and morphology while simultaneously suppressing the formation of deleterious phases (e.g., Laves phases, sigma phases) within a practical processing window remains a significant challenge. This complexity demands sophisticated thermodynamic and kinetic modeling, coupled with extensive experimental validation, to effectively navigate the vast compositional space.

Based on the aforementioned design principles, Daniel et al. [56] proposed an optimized composition with superior overall performance: $Fe_{bal}Cr_9Ni_4Si_2(Mn_{0.6}Zr_{0.4})_{1.2}$ at.%. The advantage of this composition lies in its ability to precipitate the G-phase at 773 K with an exceptionally rapid aging response. G-phase precipitation effectively leads to significant strengthening, manifested by a substantial hardness increment of approximately 60 HV.

Thermodynamic phase diagram calculations by Yang et al. [49] (Figure 5) revealed that the concentrations of Ni, Si, and alloying element X serve as critical thermodynamic levers for controlling G-phase precipitation and the resulting microstructure. The calculations predicted that a high (Ni + Si) content (e.g., 5Ni + 5Si, wt.%) combined with a moderate X concentration (~1.5 wt.%) defines an optimal compositional window. This window maximizes the G-phase volume fraction and broadens its stability

across a wide temperature range (900–1100 °C) while effectively suppressing the formation of deleterious Laves phases. This theoretical prediction provided a strategic direction for designing G-phase strengthened steels with superior high-temperature stability. Subsequent experiments confirmed that alloys designed based on these calculations (e.g., XD-2Ti) achieved the expected high number density of nanoscale G-phase precipitates and significant age-hardening, demonstrating the high reliability and practical value of thermodynamic modeling in the design of advanced high-performance steels.

Despite their undeniable utility, the predictive capabilities of thermodynamic calculations (CALPHAD) and DFT in G-phase steel design are subject to several critical limitations that warrant a more in-depth discussion. Firstly, the accuracy and completeness of the underlying thermodynamic databases are paramount. Commercial CALPHAD databases, while extensive, may not always contain robust descriptions for all relevant G-phase variants or accurately capture their interactions with other complex phases, especially in multi-component systems or under non-equilibrium conditions. The extrapolation of data beyond validated ranges can lead to significant discrepancies between predictions and experimental observations. Similarly, DFT calculations, while providing fundamental insights into electronic structure and bonding, often operate under ideal conditions (e.g., 0 K, perfect periodicity) and may not fully account for the complex interplay of temperature-dependent entropy effects, defects, and local chemical environments that influence phase stability and formation at processing temperatures.

Secondly, and perhaps most critically, both CALPHAD and DFT are primarily equilibrium-based or ground-state prediction tools. They are inherently limited in their ability to predict precipitation kinetics—the time-dependent evolution of phases, including nucleation rates, growth rates, and coarsening behavior. The formation of G-phase, like many other strengthening precipitates, is a kinetically controlled process. A thermodynamically stable phase may not form readily if the kinetic barriers are too high, or a metastable phase might precipitate first and dominate the microstructure. The absence of robust kinetic modeling means that while these tools can identify promising compositional windows for G-phase stability, they cannot fully predict the optimal aging temperatures and times required to achieve a desired precipitate size, number density, and distribution, which are crucial for maximizing strengthening and ductility. This necessitates extensive experimental validation and optimization, as computational results should be utilized primarily as a preliminary guidance tool. Consequently, computational results must be integrated with rigorous experimental validation to ensure cross-verification and refinement, thereby reliably advancing the development of novel high-performance alloys.

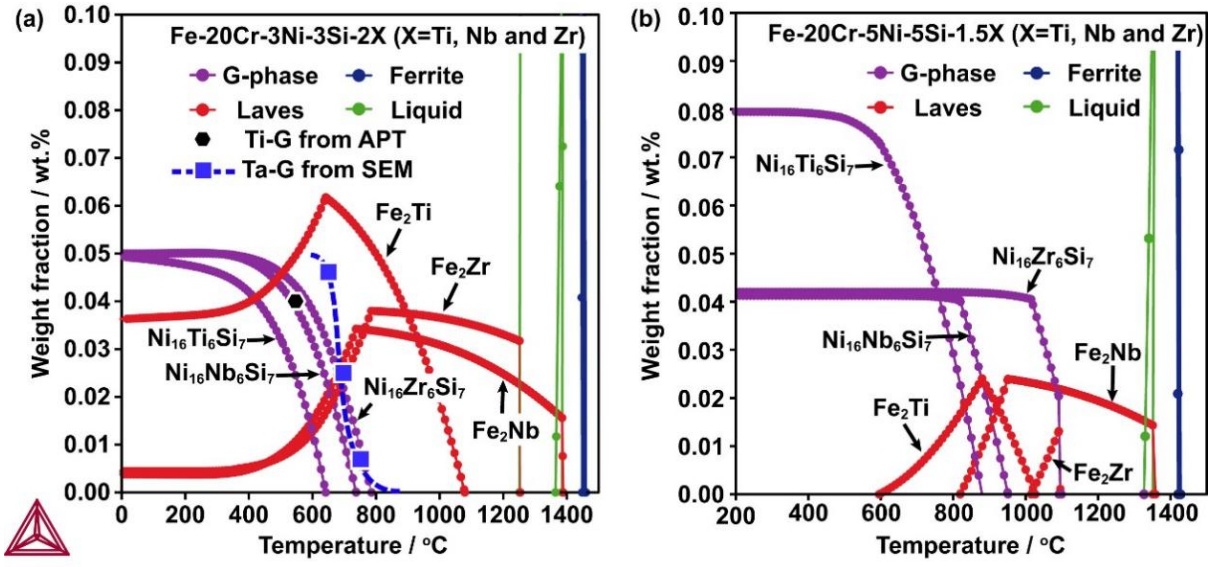

Figure 5. Predicted phase fractions as a function of temperature for Fe-20Cr multi-component alloy systems calculated using thermodynamic databases: (**a**) Fe-20Cr-3Ni-3Si-2X; (**b**) Fe-20Cr-5Ni-5Si-1.5X (where X = Ti, Nb, and Zr).

3. Precipitation Behavior of G-Phase

Nanoscale precipitation is a well-established strategy for enhancing the strength and ductility of advanced metallic materials, as exemplified by Cu-rich precipitates in maraging steels or oxide dispersions in ODS alloys. These precipitates typically form through various mechanisms, influencing their morphology, distribution, and interaction with dislocations. Extensive transmission electron microscopy (TEM) and atom probe tomography (APT) observations consistently demonstrate that the G-phase, a unique silicide, also precipitates as nanoscale particles dispersed within the ferritic matrix. These precipitates maintain a cube-on-cube orientation relationship with the matrix, defined as $(001)_G//(001)_\alpha$ and $(110)_G/(110)_\alpha$ [49] (Figure 6). This specific low-energy interfacial structure, akin to the coherent or semi-coherent interfaces observed in many precipitation-strengthened alloys, effectively suppresses the coarsening of the G-phase particles. However, distinct differences in intragranular precipitation behavior are observed among different G-phase types, and these behaviors present both commonalities and unique aspects when compared to other well-known strengthening precipitates.

3.1. Dispersed Intragranular Precipitation

The distinct differences in intragranular precipitation behavior are observed among different G-phase types: (1) $Ni_{16}Mn_6Si_7$-G phase: In the Fe-20Cr-3Ni-3Si-2Mn alloy, G-phase precipitation is sluggish. Cold-rolling pretreatment followed by aging at 400–500 °C is required to facilitate intragranular precipitation [50] (Figure 7). This sluggish kinetics contrasts with the rapid precipitation observed in some carbide- or B2-strengthened steels, highlighting a challenge in G-phase systems that often necessitates specific thermomechanical treatments. The $Ni_{16}Mn_6Si_7$-G phase exhibits spherical or cuboidal morphologies, with its size evolving with aging time: after aging at 400 °C for 90 days, the size remains below 10 nm, whereas it increases to 40–50 nm after 90 days at 500 °C. The precipitates are distributed along intragranular dislocation lines, indicating that defects introduced by cold rolling provide the necessary nucleation sites. (2) $Ni_{16}Ti_6Si_7$-G phase: In the Fe-20Cr-3Ni-3Si-1Mn-2Ti alloy, the G-phase precipitates rapidly within 24 h of aging at 560 °C, forming nanoscale spherical particles with a size of approximately 8–10 nm. These precipitates are fully coherent with the matrix (Figure 8). Such rapid, coherent precipitation kinetics are reminiscent of those of Cu-rich precipitates in maraging steels, which also form quickly and contribute significantly to strengthening. The core of the G-phase consists of a non-stoichiometric $(Fe, Ni)_{16}Ti_6Si_7$ composition containing approximately 10 at.% Fe [50]. Interestingly, the core of the $Ni_{16}Ti_6Si_7$-G phase is frequently enveloped by an $L2_1$-type Heusler phase (Fe_2TiSi), forming a unique "core-shell" structure. Both phases maintain a cube-on-cube orientation relationship with the matrix. Furthermore, the envelopment by the Fe_2TiSi shell appears to be incomplete, characterized by a persistent "broken corner" (Figure 8c). To visually elucidate this intricate microstructural arrangement, a schematic diagram illustrating the $Ni_{16}Ti_6Si_7$-G phase core enveloped by the $L2_1$-type Heusler shell is presented in Figure 9. This complex core-shell morphology is a distinctive feature of the Ti-containing G-phase system, differing from the single-phase precipitates typically found in many other strengthening systems (e.g., simple carbides or nitrides), and suggests intricate co-precipitation mechanisms. This structural feature is hypothesized to be related to the crystalline anisotropy of the two phases; however, no research progress has been reported on this specific phenomenon to date. (3) $Ni_{16}Nb_6Si_7$ and $Ni_{16}Ta_6Si_7$ G-phases: These two types of G-phases exhibit a uniform intragranular dispersion throughout the matrix. Their characteristic sizes are significantly larger than those of the $Ni_{16}Ti_6Si_7$-G phase ($Ni_{16}Nb_6Si_7$ is approximately 6.5 nm and $Ni_{16}Ta_6Si_7$ is approximately 25 nm), and the particle compositions reach equilibrium within 24 h of aging. APT analysis confirmed that these precipitates possess a $(Fe, Ni)_{16}M_6Si_7$ (M = Nb or Ta) stoichiometry, with an exceptionally high Fe content of approximately 30 at.% (surpassing the Ni concentration) [50]. This significant Fe substitution for Ni sites offers a strategic roadmap for developing cost-effective, low-Ni or

Ni-free G-phase strengthened steels, analogous to compositional optimization strategies employed in other advanced alloys to reduce reliance on expensive or critical elements. This demonstrates that Fe can occupy Ni sites, providing a strategic roadmap for the development of cost-effective, low-Ni or Ni-free G-phase strengthened steels.

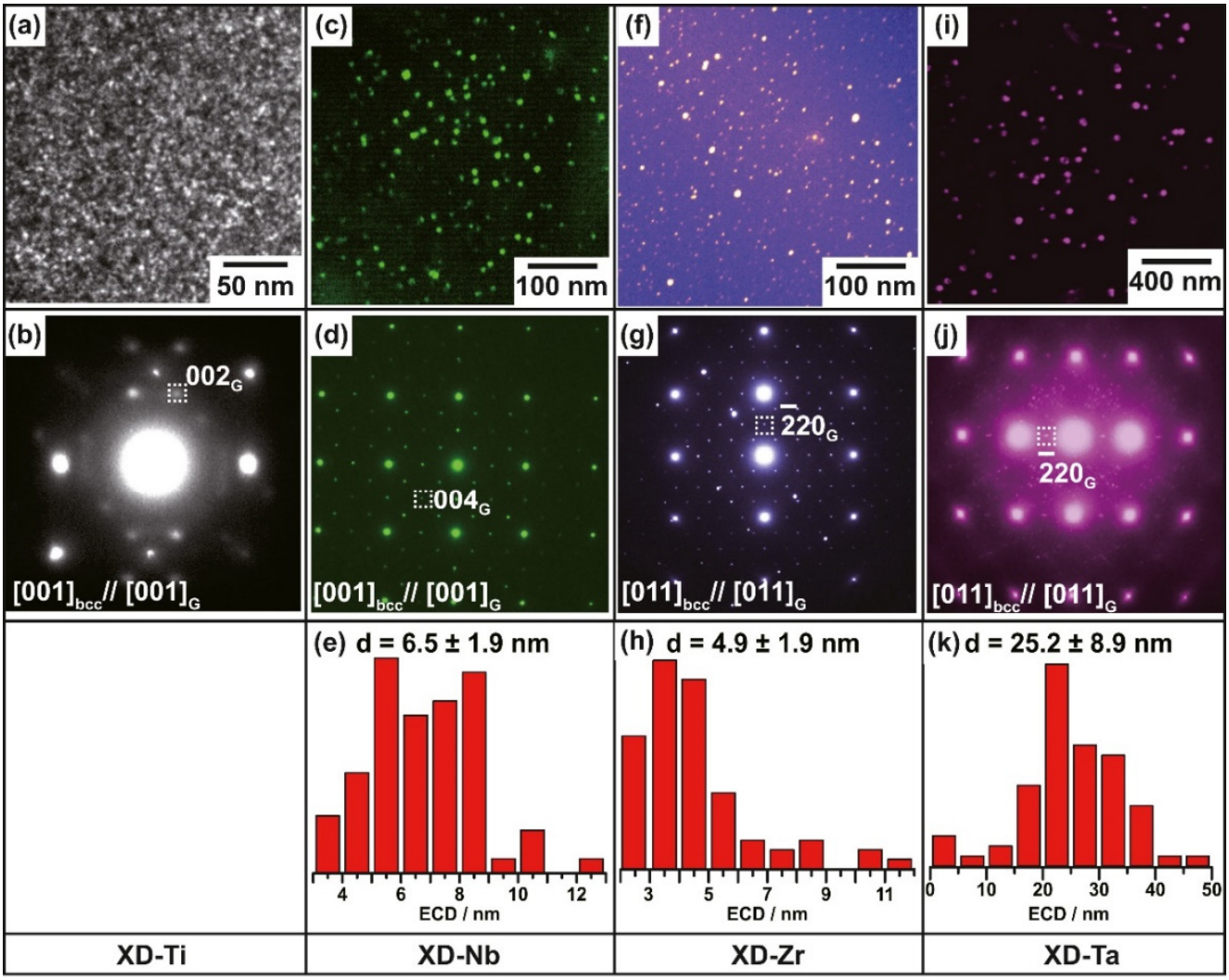

Figure 6. Typical TEM micrographs of four foundational G-phase strengthened alloys. (**a**,**c**,**f**,**i**) Dark fields images; (**b**,**d**,**g**,**j**) corresponding diffraction patterns; (**e**,**h**,**k**) corresponding statistic particle distributions . Note that the ECD in (e) to (k) means the equivalent circular diameter of these fine precipitate particles.

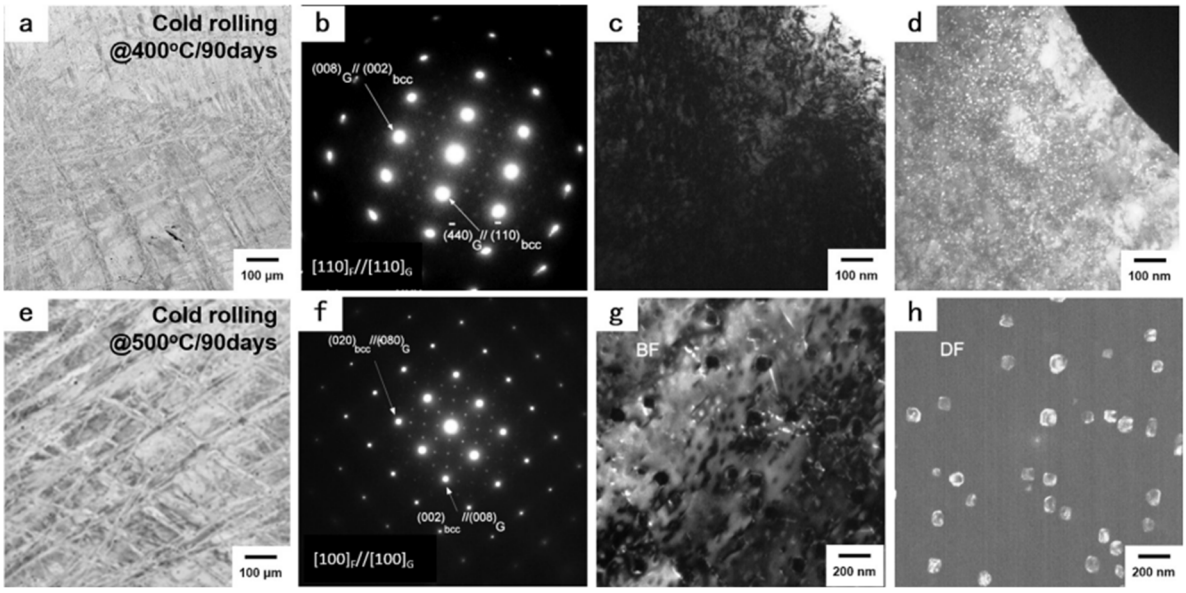

Figure 7. TEM micrographs showing the microstructure of $Ni_{16}Mn_6Si_7$-G phase strengthened steel. (**a**,**e**) back-scattered-electron (BSE) images; (**b**,**f**) selected area electron diffraction (SAED) from the 110F and 100F incident, respectively; (**c**,**g**) bright field (BF) images; (**d**,**h**) dark field (DF) images taken from the -220$_G$ spot in Fig. 7b and the 040$_G$ in Fig. 7f, respectively.

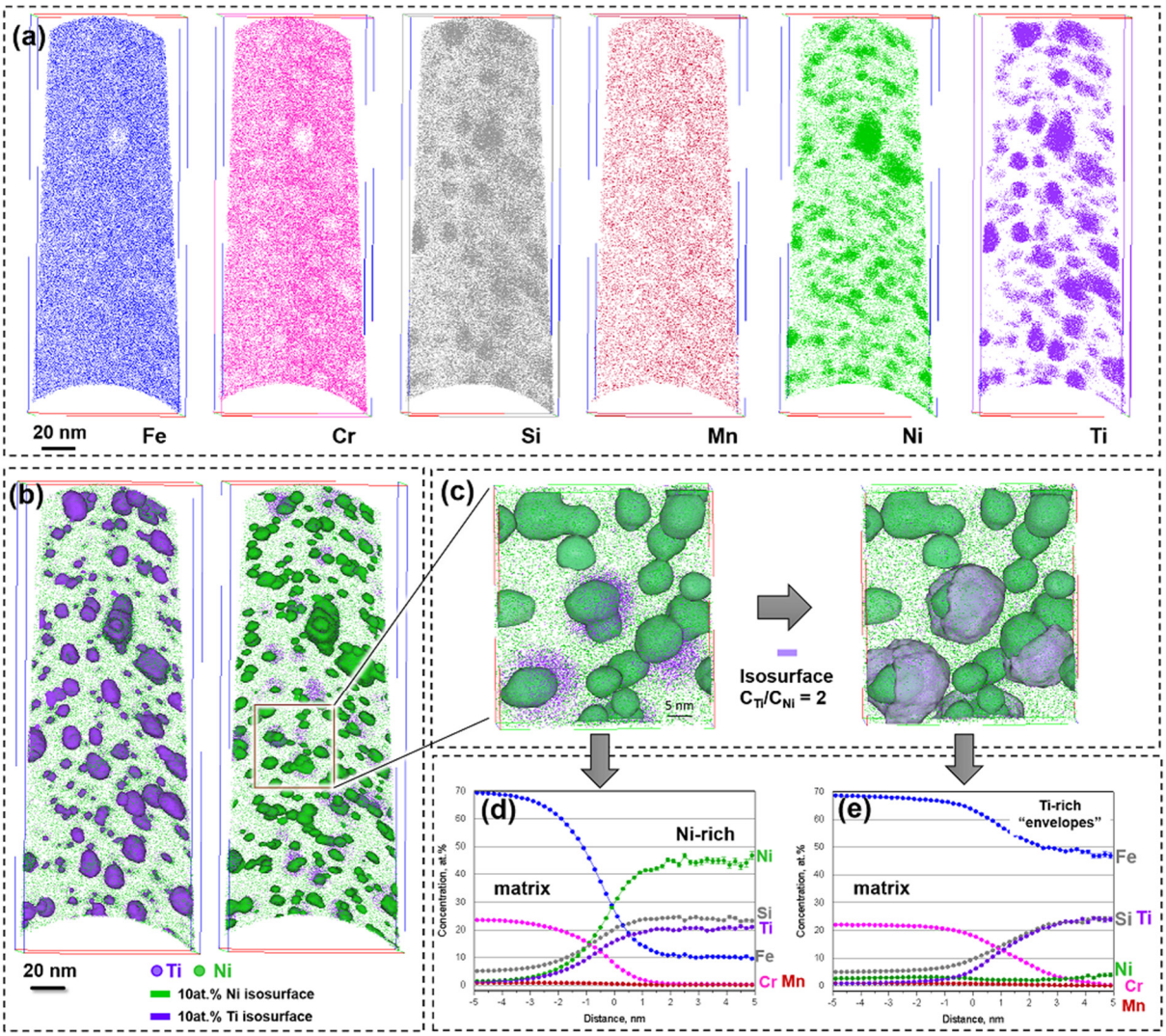

Figure 8. Three-dimensional atom probe tomography analysis of the $Ni_{16}Ti_6Si_7$-G phase strengthened 20Cr stainless steel (2Ti). (**a**) 20 nm thick slice from atom maps for Fe, Cr, Si, Mn, Ni and Ti; (**b**) atom maps with isosurfaces of the 10 at.% Ti and 10 at.%

Ni; (**c**) enlarged image from (**b**) with a corresponding isosurface of the CTi/CNi = 2; (**d**) the composition profiles from the matrix to the Ni-rich phase; (**e**) the composition profiles from the matrix to the Ti-rich "envelope" phase.

A comprehensive comparison reveals distinct differences in the precipitation behavior of various G-phase types. In terms of precipitation kinetics, $Ni_{16}Ti_6Si_7$ exhibits the most rapid kinetics (occurring in less than 24 h), whereas $Ni_{16}Mn_6Si_7$ is the most sluggish (requiring 60–90 days). The kinetics of $Ni_{16}Nb_6Si_7$ and $Ni_{16}Ta_6Si_7$ fall in between these extremes. These variations are primarily attributed in the literature to differences in the enthalpy of formation across the different alloying systems. Regarding precipitate characteristics, the $Ni_{16}Ti_6Si_7$-G phase features the finest size (with a radius of 1.6 nm) and the highest number density (~6×10^{23} m^{-3}). In contrast, the $Ni_{16}Nb_6Si_7$ and $Ni_{16}Ta_6Si_7$ variants exhibit larger particle sizes but possess superior thermal stability. Notably, only the Ti-based system develops the $L2_1$-enveloped core-shell structure, while other G-phases precipitate as a single phase, suggesting that Ti additions introduce complex phase transformation pathways. These findings provide a microstructural foundation for designing high-strength G-phase strengthened steels, indicating that precipitation behavior can be precisely tuned in the future by optimizing the combination of G-phase forming elements.

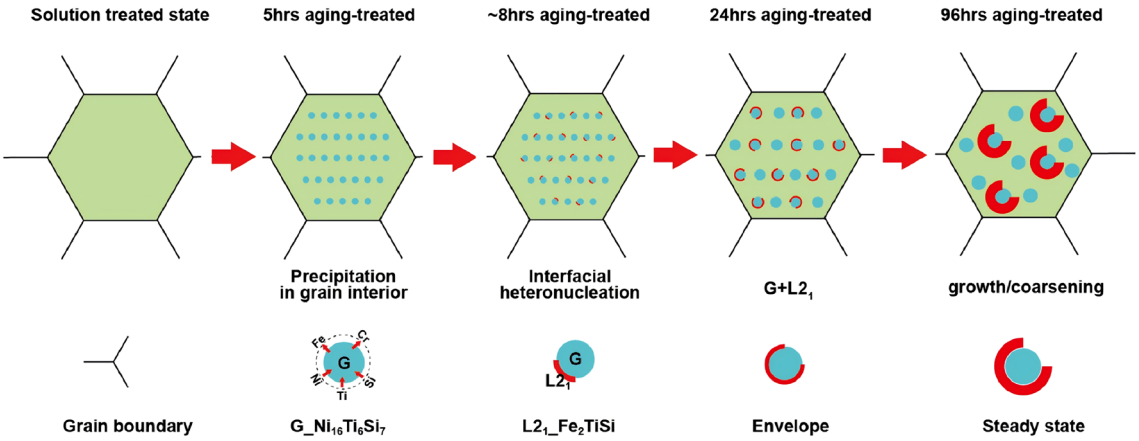

Figure 9. Schematic of the formation of a core-shell structure in the 2Ti alloy during aging at 560 °C.

3.2. Extensive Grain Boundary Precipitation

The G-phase is named for its characteristic precipitation along grain boundaries in austenitic stainless steels [57]. Similarly, in ferritic stainless steels, the G-phase exhibits a pronounced tendency for grain boundary precipitation, which often triggers brittle fracture. Key findings from the author's research group are summarized as follows [58]: (1) Early stage of aging: (e.g., aging at 550 °C for 1 h), a segregation layer enriched in Ni, Ti, and Si (with the exclusion of Fe and Cr) forms along the grain boundaries, measuring approximately 6 nm in width, though no distinct precipitates are yet detectable. (2) Evolution of precipitates: With prolonged aging (e.g., 48 h), this segregation layer transforms into a continuous $(Ni, Fe)_{16}Ti_6Si_7$-G phase. Interestingly, the grain boundary G-phase tends to maintain a cube-on-cube orientation relationship with only one of the adjacent ferrite grains, eventually covering the entire grain boundary area (Figures 10 and 11).

The intergranular embrittlement observed in G-phase strengthened steels is a critical limitation, primarily attributed to the formation of continuous G-phase films along grain boundaries. This continuous network acts as a preferential path for crack initiation and propagation under stress, leading to brittle fracture. The disparity between intragranular and grain boundary precipitation behaviors, where the G-phase at grain boundaries often exhibits a coarser, less coherent morphology compared to its intragranular counterparts, exacerbates this issue. This mismatch prevents the uniform transmission of stress and strain across the interface, leading to localized stress concentrations and the initiation of intergranular cracks [58]. Furthermore, the specific morphology and crystallography of grain boundary G-phase precipitates—

particularly their tendency to maintain coherency with only one adjacent grain—can significantly alter interfacial energy, thereby elevating susceptibility to brittle intergranular failure; this behavior mirrors the well-documented embrittlement mechanisms observed in other alloy systems containing deleterious grain boundary phases, such as carbides or sigma phases in stainless steels, underscoring the broad relevance of grain boundary engineering for mitigating precipitation-induced intergranular embrittlement across diverse structural alloys.

Cold-rolling pretreatment has proven effective in suppressing the intergranular precipitation of the G-phase, thereby enhancing ductility. This currently serves as the primary processing strategy to circumvent brittle cracking in G-phase strengthened ferritic stainless steels [58]. Figure 12 provides a schematic illustration of this critical microstructural control mechanism. The underlying microstructural mechanism is that cold-rolling introduces a high density of dislocations and deformed sub-grains, which act as preferential sites for G-phase precipitation during aging (intragranular precipitation), effectively bypassing the grain boundaries (Figure 13). This strategy, where cold-rolling introduces a high density of defects to promote intragranular precipitation, is a well-established approach in materials science, similar to its application in some maraging steels to refine precipitate distribution.

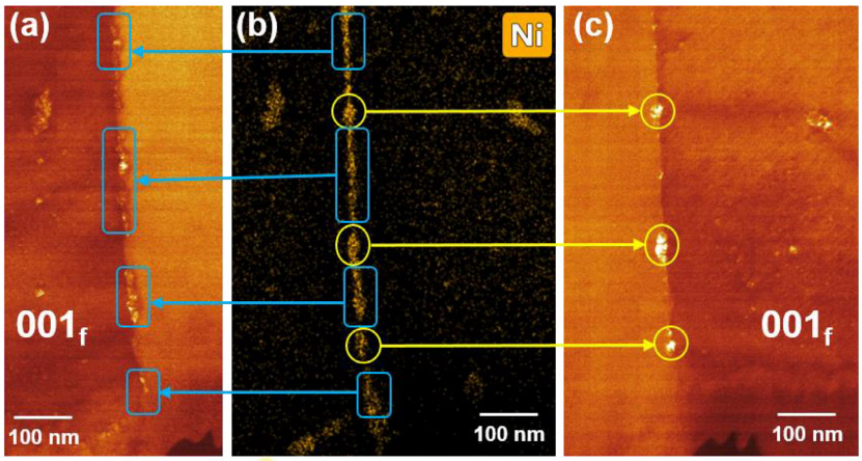

Figure 10. Grain boundary precipitates in the $Ni_{16}Ti_6Si_7$-G phase strengthened 20Cr stainless steel (1Ti). (**a**) dark field micrograph of the left grain (ZA = 001_f); (**b**) EDS-mapping result of elemental Ni on grain boundary; (**c**) dark field micrograph of the right grain (ZA = 001_f).

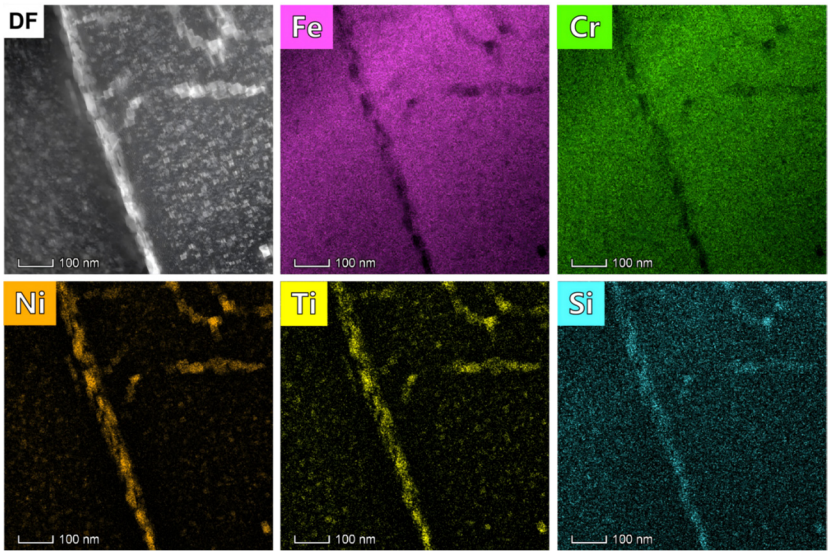

Figure 11. Compositional analysis of grain boundary precipitates in the $Ni_{16}Ti_6Si_7$-G phase strengthened 20Cr stainless steel (1Ti).

While effective in laboratory settings, the industrial feasibility of extensive cold-rolling as a universal mitigation strategy for G-phase steels presents significant constraints. Large or complex-shaped components are difficult to cold-roll uniformly, and the process itself can introduce substantial residual stresses, potentially requiring additional post-processing steps. Moreover, the energy and cost associated with large-scale cold-rolling operations can be prohibitive for certain industrial applications. Therefore, despite its demonstrated success in eliminating continuous intergranular G-phase, the reliance on extensive cold-rolling significantly limits the processability and industrial versatility of these materials. Consequently, there remains an urgent need to explore more efficient, scalable, and cost-effective strategies, such as micro-alloying or novel heat treatments, to expand the practical application potential of this class of high-strength steels without compromising industrial viability.

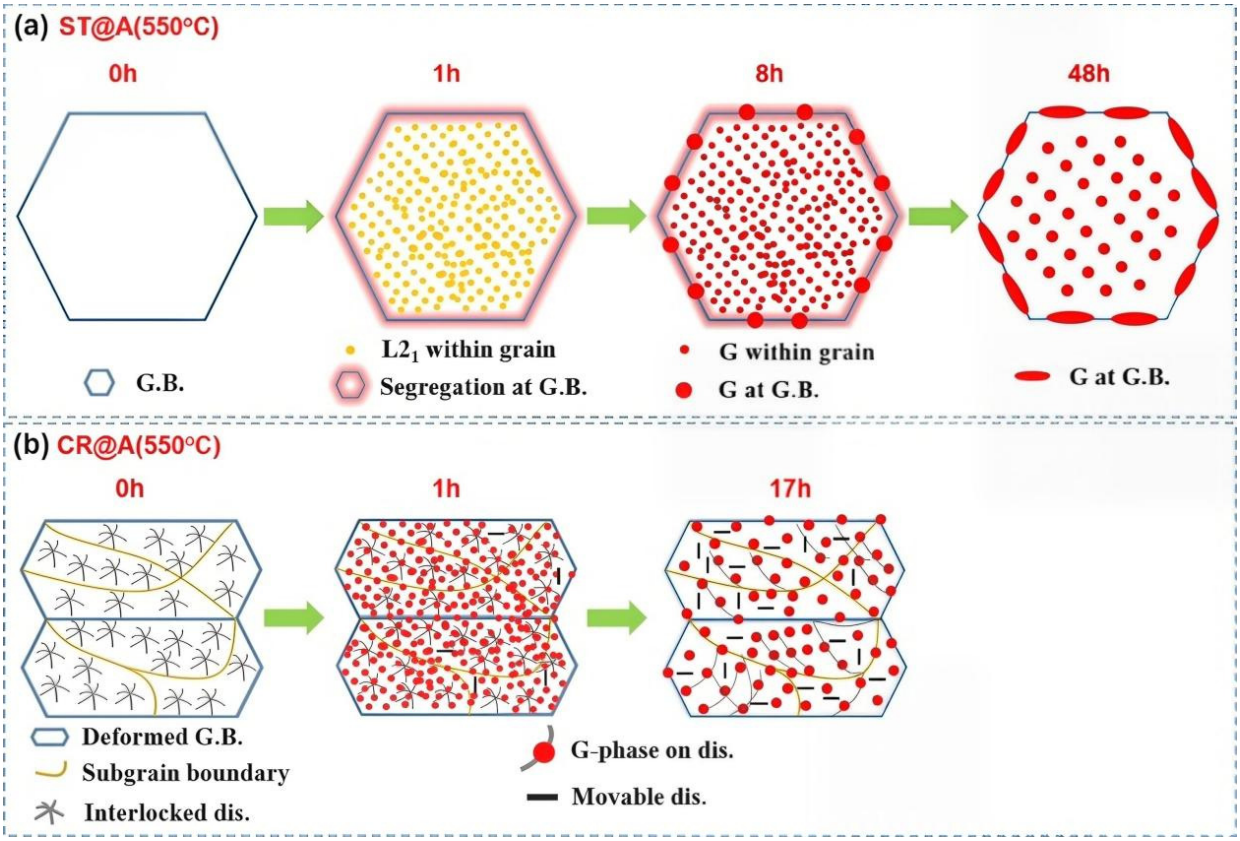

Figure 12. Illustrative comparison of precipitation behavior differences under two treatment conditions: (**a**) Solution treated@Aging treatment; (**b**) Cold Rolled@Aging treatment.

DFT calculations further elucidate the thermodynamic mechanisms governing G-phase precipitation at grain boundaries [58]. The low interfacial energy between the G-phase and the ferrite matrix (e.g., the Fe(111)||G(111) interface) facilitates heterogeneous nucleation at defects such as grain boundaries and dislocations. The calculations reveal that this low interfacial energy corresponds to a high work of adhesion, indicating a robust interfacial bonding strength. Furthermore, the introduction of dislocations via cold-rolling provides alternative nucleation sites, thereby promoting a more dispersed intragranular precipitation and suppressing detrimental grain boundary coverage.

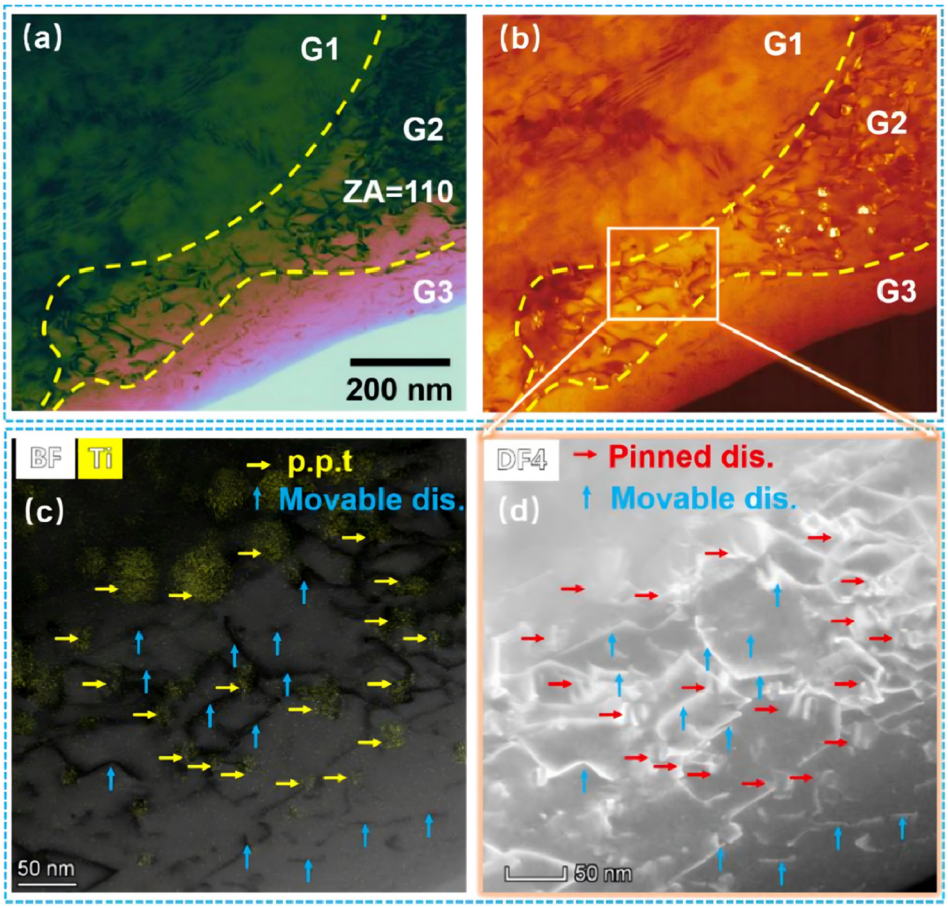

Figure 13. Typical microstructure of the $Ni_{16}Ti_6Si_7$-G-phase strengthened 20Cr stainless steel after cold-rolling and subsequent aging treatment. (**a**) bright field (BF) micrograph showing the microstructure of three adjacent deformed grains (the zone axis (ZA) for grain 2 is exactly [110] while that of the other two is far from [110]); (**b**) corresponding dark field (DF) micrograph; (**c**) Ti-distribution map decorated BF micrograph; (**d**) corresponding high angle annular dark field (HAADF) micrograph.

4. Mechanical Properties

The evolution of hardness directly reflects the precipitation hardening response of the G-phase. Our studies on $Ni_{16}X_6Si_7$-G phase strengthened alloys aged at 560 °C demonstrated that the peak hardness follows the sequence [49]: Ti (620 HV) >> Nb (410 HV) > Ta (390 HV) >> Zr (310 HV). Specifically, the Ti-containing alloy reaches its peak hardness within 8–10 h. In contrast, the peak for the Ta-containing alloy is delayed to 24 h due to the low diffusivity of Ta. Beyond peak aging, all alloys exhibit a slight softening trend, which is attributed to the Ostwald ripening of G-phase particles (Figure 14). In the case of $Co_{16}X_6Si_7$-G phase strengthened alloys aged at 600 °C, all variants (X = Ti, Nb, Ta) undergo rapid age-hardening within the first hour [55]. Furthermore, cold-rolling pre-deformation can boost the peak hardness to 435–455 HV, yielding a significant hardness increment (ΔHV) of approximately 160 HV. These results demonstrate that Co-based G-phases also possess substantial strengthening potential.

When critically comparing these hardness values with other advanced high-strength steels, G-phase strengthened ferritic stainless steels demonstrate competitive performance. For instance, the peak hardness of 620 HV for the Ti-containing G-phase alloy is comparable to or even surpasses that of many advanced maraging steels (e.g., 500–650 HV for some 18Ni maraging steels) and certain nanoprecipitate-hardened high-entropy alloys [59]. This highlights the significant strengthening efficiency of the G-phase. However, it is imperative to note that the kinetics of age-hardening and the specific strengthening mechanisms (e.g., shearing *vs*. bypassing of precipitates) can differ substantially across these material classes, influencing their overall performance and application suitability.

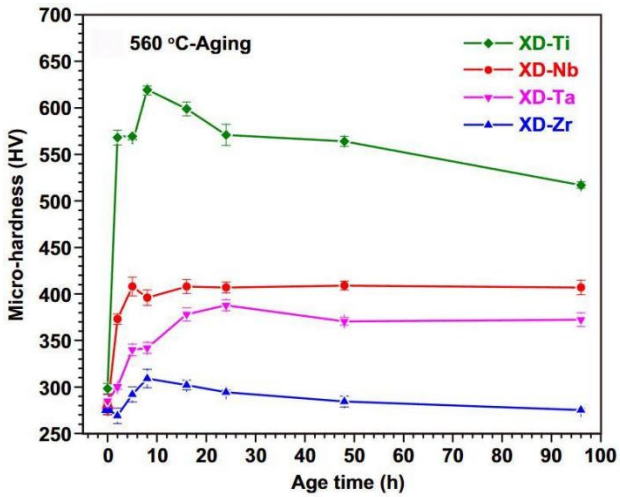

Figure 14. Aging hardness curves of four different G-phase strengthened ferritic stainless steels.

The primary technical bottleneck for G-phase strengthened Fe-20Cr ferritic stainless steels is their poor tensile ductility. Some alloys even undergo intergranular brittle fracture, which significantly restricts their development and practical application (Figure 15). This brittle behavior is a critical concern, and its mechanistic understanding is crucial for alloy design. Fractographic analyses from various studies [58] consistently reveal that the fracture mode in solution-aged G-phase steels is predominantly intergranular. This is directly linked to the continuous G-phase precipitation along grain boundaries, as discussed in Section 3.2. These brittle G-phase films act as preferential sites for crack nucleation under tensile stress. Once initiated, cracks propagate along these weakened grain boundaries, leading to catastrophic failure with minimal plastic deformation. The lack of uniform stress transfer across the G-phase decorated grain boundaries, coupled with the inherent brittleness of the G-phase itself, contributes to this severe embrittlement. This mechanism is analogous to intergranular fracture observed in other alloy systems, in which brittle phases (e.g., carbides, sigma phases) form continuously along grain boundaries.

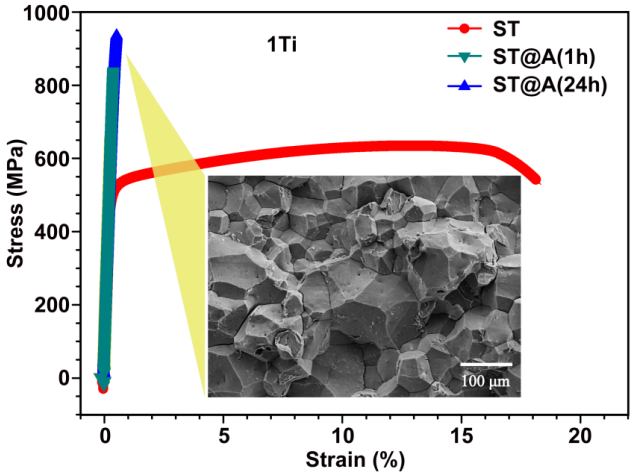

Figure 15. Tensile stress-strain curves exhibiting brittle fracture in the $Ni_{16}Ti_6Si_7$-G phase strengthened 20Cr stainless steel after solution and subsequent aging treatment.

However, by employing a cold-rolling and subsequent aging process, the strength-ductility trade-off can be effectively resolved [58] (Figure 16). This improvement is not merely an empirical observation but stems from a fundamental shift in the precipitation behavior and subsequent deformation mechanisms. Cold-rolling introduces a high density of dislocations and sub-grain boundaries, which serve as heterogeneous nucleation sites for the G-phase during subsequent aging. This promotes a more uniform,

intragranular dispersion of fine G-phase precipitates, effectively suppressing the formation of continuous grain boundary films. Consequently, the deformation mechanism shifts from brittle intergranular fracture to more ductile modes involving dislocation-precipitate interactions. Specifically, the cold-rolled and aged alloys exhibit:

(1) Ultra-high strength: After aging at 550 °C for 1 h, the alloy achieves an ultra-high yield strength of ~1700 MPa while maintaining a total elongation of 4%. This remarkable strength is primarily attributed to the high number density and fine size of the intragranular G-phase precipitates, which act as potent obstacles to dislocation motion. The strengthening mechanism is likely a combination of Orowan looping and particle shearing, depending on the precipitate size and coherence with the matrix, similar to mechanisms observed in other nanoprecipitate-hardened steels [60,61].

(2) Excellent strength-ductility balance: Aging at 600 °C for 12 h results in a tensile strength of ~1300 MPa and an elongation of ~10%, demonstrating an outstanding comprehensive performance. To quantitatively assess this balance, the strength-ductility product (SDP), defined as the product of ultimate tensile strength and total elongation, can be used. For these G-phase steels, the SDP values achieved after optimized cold-rolling and aging are competitive with, and in some cases surpass, those of other advanced high-strength steels, including certain maraging steels and high-entropy alloys [62–64]. This synergy is achieved by mitigating grain boundary embrittlement while maintaining effective intragranular precipitation strengthening.

(3) Improved bending performance: The cold-rolled and aged specimens exhibit bending angles ranging from 40° to 85°. In sharp contrast, the solution-aged specimens exhibit a bending angle of 0° and fracture immediately upon loading. This drastic improvement in bending ductility further underscores the effectiveness of the cold-rolling strategy in enhancing the material's resistance to localized deformation and fracture.

This challenge of maintaining ductility while achieving ultra-high strength is a pervasive issue in materials science, particularly in many nanoprecipitate-hardened systems where high precipitate volume fractions can lead to embrittlement. For example, while some maraging steels achieve exceptional strength, their ductility can be sensitive to precipitate morphology and distribution. Similarly, ODS steels, despite their excellent high-temperature strength, often exhibit limited ductility at room temperature. The strategy of using cold-rolling to resolve the strength-ductility trade-off in G-phase steels, by promoting intragranular precipitation and mitigating grain boundary embrittlement, represents a significant advancement. This approach is analogous to thermomechanical processing routes employed in other advanced steels to optimize precipitate distribution and enhance toughness [65]. However, the requirement for extensive cold-rolling still poses practical limitations, necessitating further research into alternative ductility enhancement strategies, such as micro-alloying or novel heat treatments, as discussed in Section 5.

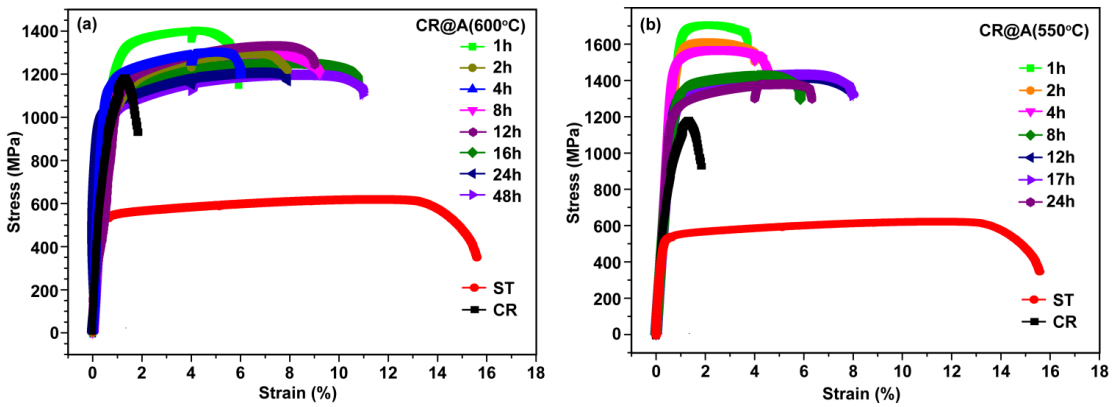

Figure 16. Tensile stress-strain curves of the $Ni_{16}Ti_6Si_7$-G phase strengthened 20Cr stainless steel after cold-rolling and subsequent aging treatment.

The high-temperature stability of the G-phase is a critical factor governing the creep resistance and elevated-temperature strength of these alloys, both of which are vital for high-temperature structural applications. In quasi-static compression tests conducted at 660 °C, the G-phase strengthened alloys exhibit excellent deformation resistance (Figure 17). Specifically, the threshold stress for the $Ni_{16}Ti_6Si_7$-G phase and $Ni_{16}Nb_6Si_7$-G phase strengthened alloys is approximately 140 MPa and 116 MPa, respectively [49]. These values surpass those of both the B2-NiAl strengthened FBB8 steel (~112 MPa) and the commercial heat-resistant steel P92. This superior creep resistance is mechanistically attributed to the high thermal stability and low coarsening kinetics of the G-phase precipitates at elevated temperatures. The fine, dispersed G-phase particles effectively pin dislocations and impede their movement, thereby hindering creep deformation. The comparison with P92 steel, a benchmark for high-temperature applications, highlights the potential of G-phase steels in environments where creep resistance is paramount. Further quantitative analysis of creep mechanisms, such as power-law creep exponents and activation energies, from future studies will provide deeper insights into the high-temperature deformation behavior. Beyond these findings, further systematic reports on the high-temperature performance of G-phase strengthened steels remain scarce.

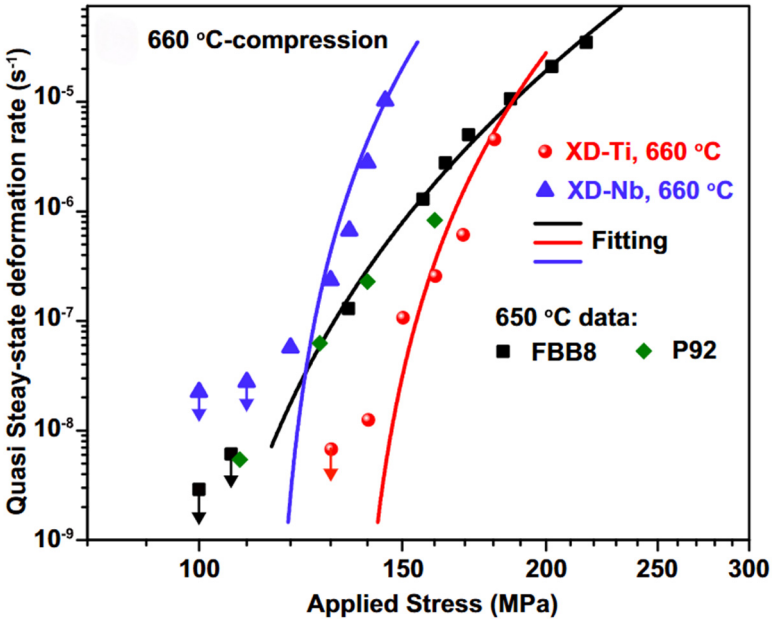

Figure 17. Quasi-static compressive creep behavior of $Ni_{16}Ti_6Si_7$-G and $Ni_{16}Nb_6Si_7$-G phase strengthened 20Cr stainless steels.

5. Future Perspectives

Based on the current state of research, future work on nano-G-phase dispersion-strengthened ferritic stainless steels should focus on the following multi-dimensional breakthroughs:

5.1. Mechanistic Research

Deepening mechanistic understanding is crucial for G-phase strengthened steels, requiring expanded phase diagram databases, first-principles calculations for metastable G-phases, and optimized aging windows for low-mismatch dispersion. Crucially, future efforts must focus on incorporating and developing advanced kinetic modeling approaches (e.g., phase-field simulations, CALPHAD-based kinetic models, or Monte Carlo methods) to predict the time-temperature-transformation (TTT) and continuous-cooling-transformation (CCT) diagrams for G-phase precipitation. This will enable a more comprehensive understanding of nucleation, growth, and coarsening kinetics, bridging the gap between thermodynamic

predictions and actual microstructural evolution, thereby facilitating the design of optimal heat treatment processes. Key unresolved questions include: why G-phase achieves superior low misfit, possibly due to internal strain accommodation within its large unit cell; how to overcome the sluggish kinetics of $Ni_{16}Mn_6Si_7$-G phase precipitation beyond cold-rolling, perhaps via high-frequency pulsed electric treatment; whether dislocations can shear ultra-fine G-phase particles; and if brittle G-phase exhibits plasticity when scaled down below 2 nm. Addressing these fundamental questions is vital for refining alloy design and fully realizing the potential of these ferritic stainless steels.

5.2. Compositional Design

Future compositional design should prioritize low-cost alloy development, such as low-Ni or Ni-free alloys achieved by substituting Fe for Ni sites, alongside optimizing X-elements (Ti, Zr, Nb, *etc*.) and Si content to maximize G-phase volume fraction while suppressing detrimental phases. Among promising systems, the Ni–Mn–Si–G phase system is particularly attractive due to the absence of competing detrimental phases like the Laves phase. However, its poor thermal stability, necessitating lower aging temperatures for precipitation, highlights the critical need to enhance its high-temperature stability. Conversely, the Ni–Ti–Si system offers the most potent G-phase strengthening effect but presents challenges due to the competitive precipitation of multiple phases ($L2_1$, G, Laves), making it highly sensitive to compositional variations. Regardless of the specific system, silicon content must be strictly controlled below 1 wt.% to ensure satisfactory overall toughness and weldability of the steel. For enhanced thermal stability and creep resistance, the Ni–Nb–Si and Ni–Ta–Si systems are superior, and appropriately increasing Nb and Ta content can further improve the overall creep performance.

5.3. Application Level

G-phase strengthened ferritic stainless steels show significant promise for next-generation 700 °C high-temperature steam pipelines in advanced thermal power plants. Increasing operating temperatures from 600 °C to 700 °C is crucial for enhancing power generation efficiency, driving demand for new heat-resistant steels. Unlike austenitic steels, which suffer from higher thermal expansion and lower thermal conductivity, leading to weld cracking, ferritic G-phase steels offer inherent advantages in mitigating thermal stress. While excellent deformation resistance has been demonstrated at 660 °C, their long-term high-temperature strength, creep, and fatigue properties at 700 °C remain largely unexplored. Therefore, future research must focus on systematic evaluation of these properties and optimizing alloy design for 700 °C service conditions to realize their full potential in high-temperature applications.

Acknowledgments

All authors gratefully acknowledge the assistance from Y. Qiu and D. He at SUStech Core Research Facilities and the electron microscope center of KAIPLE Co., Ltd. (Changsha, China) for the support of microstructural characterizations.

Author Contributions

M.Y.: Conceptualization, Methodology, Funding acquisition, Supervision, Literature review, Writing—original draft, Writing—review & editing. D.Z. (Daobin Zhang): Literature review, Writing—original draft. J.Y.: Funding acquisition, Literature review. Z.Y.: Methodology, Literature review. D.Z. (Dingding Zhu): Literature review, Writing—review & editing. B.D.: Literature review. M.H.: Funding acquisition, Literature review. S.W.: Literature review, Writing—review & editing. C.W.: Literature review, Writing—review & editing. X.L.: Conceptualization, Funding acquisition, Literature revie, Writing—review & editing.

Ethics Statement

Not applicable.

Informed Consent Statement

Not applicable.

Data Availability Statement

No new data were generated or analyzed in this study. All information is available within the cited references.

Funding

M.Y. acknowleges the support from the Guangdong Basic and Applied Basic Research Foundation (Grant No. 2023A1515240048), the Shenzhen Science and Technology Program (Grant No. JCYJ20240813094806009) and the National Natural Science Foundation of China (Grant No. 52301153); J.Y. acknowleges the support from the National Natural Science Foundation of China (Grant No. 52301154) and the Shenzhen Science and Technology Program (Grant No. JCYJ20220530114400001); M.H. acknowleges the support from the Guangdong Basic and Applied Basic Research Foundation (Grant No. 2023A1515110595); Z.Y. acknowleges the support from the National Natural Science Foundation of China (Grant No. 52301042) and the Natural Science Foundation of Top Talent of SZTU (grant No. GDRC202532).

Declaration of Competing Interest

The authors declare that they have no known competing financial interests or personal relationships that could have appeared to influence the work reported in this paper.

References

1. Jiang S, Wang H, Wu Y, Liu X, Chen H, Yao M, et al. Ultrastrong steel via minimal lattice misfit and high-density nanoprecipitation. *Nature* **2017**, *544*, 460–464. DOI:10.1038/nature22032
2. He BB, Hu B, Yen HW, Cheng GJ, Wang ZK, Luo HW, et al. High dislocation density–induced large ductility in deformed and partitioned steels. *Science* **2017**, *357*, 1029–1032. DOI:10.1126/science.aan0177
3. Kwiatkowski da Silva A, Souza Filho IR, Lu W, Zilnyk KD, Hupalo MF, Alves LM, et al. A sustainable ultra-high strength Fe18Mn3Ti maraging steel through controlled solute segregation and α-Mn nanoprecipitation. *Nat. Commun.* **2022**, *13*, 2330. DOI:10.1038/s41467-022-30019-x
4. Gao J, Jiang S, Zhang H, Huang Y, Guan D, Xu Y, et al. Facile route to bulk ultrafine-grain steels for high strength and ductility. *Nature* **2021**, *590*, 262–267. DOI:10.1038/s41586-021-03246-3
5. Liu X, Liu C, Wu J, Zhang X, Zhu X, Wang J. Morphological instability of the G-phase induced a different contribution to hardening of ferrite phase in a duplex stainless steel. *Mater. Sci. Eng. A* **2022**, *832*, 142421. DOI:10.1016/j.msea.2021.142421
6. Mateo A, Llanes L, Anglada M, Redjaimia A, Metauer G. Characterization of the intermetallic G-phase in an AISI 329 duplex stainless steel. *J. Mater. Sci.* **1997**, *32*, 4533–4540. DOI:10.1023/A:1018669217124
7. Sun WW, Marceau RKW, Styles MJ, Barbier D, Hutchinson CR. G phase precipitation and strengthening in ultra-high strength ferritic steels: Towards lean 'maraging' metallurgy. *Acta Mater.* **2017**, *130*, 28–46. DOI:10.1016/j.actamat.2017.03.032
8. Zhang S, Shi X, Su Y, Yan W, Rong L, Yang K. G phase and ferrite in a high Si austenitic stainless steel during 510 °C aging. *Mater. Charact.* **2024**, *207*, 113587. DOI:10.1016/j.matchar.2023.113587
9. Zheng Y, Hu X, Jiang H, Song Y, Rong L. Precipitation behavior of G-phase and its effect on mechanical properties of 30Cr2Ni4MoV steel. *Mater. Charact.* **2025**, *219*, 114598. DOI:10.1016/j.matchar.2024.114598

10. Purzyńska H, Golański G, Zieliński A, Dobrzański JD, Sroka M. Precipitation study in Ti-stabilised austenitic stainless steel after 207,000 h of service. *Mater. High Temp.* **2019**, *36*, 296–303. DOI:10.1080/09603409.2018.1546919
11. Guo XF, Ni YY, Gong JM, Geng LY, Tang JQ, Jiang Y, et al. Formation of G-phase in 20Cr32Ni1Nb Stainless Steel and its Effect on Mechanical Properties. *Acta Metall. Sin.* **2017**, *30*, 829–839. DOI:10.1007/s40195-017-0589-0
12. Pedro Ibañez RA, de Almeida Soares GD, de Almeida LH, Le May I. Effects of Si content on the microstructure of modified-HP austenitic steels. *Mater. Charact.* **1993**, *30*, 243–249. DOI:10.1016/1044-5803(93)90071-3
13. Chen WY, Li M, Zhang X, Kirk MA, Baldo PM, Lian T. *In situ* TEM study of G-phase precipitates under heavy ion irradiation in CF8 cast austenitic stainless steel. *J. Nucl. Mater.* **2015**, *464*, 185–192. DOI:10.1016/j.jnucmat.2015.04.042
14. Lee EH, Maziasz PJ, Rowcliffe AF. *Structure and Composition of Phases Occurring in Austenitic Stainless Steels in Thermal and Irradiation Environments: CONF-801072-11*; Oak Ridge National Lab.: Oak Ridge, TN, USA, 1980.
15. Porollo SI, Konobeev YV, Garner FA. Swelling and microstructure of austenitic stainless steel ChS-68 CW after high dose neutron irradiation. *J. Nucl. Mater.* **2009**, *393*, 61–66. DOI:10.1016/j.jnucmat.2009.05.005
16. Kong BS, Shin JH, Jang C, Na YE, Jang D, Lee HJ, et al. Effect of proton irradiation on δ-ferrite in the thermally aged austenitic stainless steel weld: Precipitation of G-phase and additional hardening. *J. Nucl. Mater.* **2021**, *544*, 152656. DOI:10.1016/j.jnucmat.2020.152656
17. Lin X, Peng Q, Han EH, Ke W, Jiao Z. Irradiation-induced precipitation and inverse coarsening of G-phase in austenitic stainless steel weld metal. *Mater. Charact.* **2019**, *151*, 396–403. DOI:10.1016/j.matchar.2019.03.035
18. Badyka R, Saillet S, Emo J, Domain C, Pareige C. Effect of Ni, Mo and Mn content on spinodal decomposition kinetics and G-phase precipitation of aged model cast austenitic stainless steels. *J. Nucl. Mater.* **2021**, *555*, 153123. DOI:10.1016/j.jnucmat.2021.153123
19. Gupta H, Kapoor R, Shinde D, Makineni SK. Achieving ultra-high flow stress and hardness in a medium Mn stainless steel by the formation of strain-induced martensite and G-phase precipitates. *Scr. Mater.* **2024**, *241*, 115892. DOI:10.1016/j.scriptamat.2023.115892
20. Gemperle A, Gemperlová J, Sha W, Smith GDW. Aging behaviour of cobalt free chromium containing maraging steels. *Mater. Sci. Technol.* **1992**, *8*, 546–554. DOI:10.1179/mst.1992.8.6.546
21. Sha W, Cerezo A, Smith GDW. Phase chemistry and precipitation reactions in maraging steels: Part III. Model alloys. *Met. Trans. A* **1993**, *24*, 1241–1249. DOI:10.1007/BF02668192
22. Murayama M, Hono K, Katayama Y. Microstructural evolution in a 17-4 PH stainless steel after aging at 400 °C. *Met. Mater. Trans. A* **1999**, *30*, 345–353. DOI:10.1007/s11661-999-0323-2
23. Schober M, Schnitzer R, Leitner H. Precipitation evolution in a Ti-free and Ti-containing stainless maraging steel. *Ultramicroscopy* **2009**, *109*, 553–562. DOI:10.1016/j.ultramic.2008.10.016
24. Schnitzer R, Schober M, Zinner S, Leitner H. Effect of Cu on the evolution of precipitation in an Fe–Cr–Ni–Al–Ti maraging steel. *Acta Mater.* **2010**, *58*, 3733–3741. DOI:10.1016/j.actamat.2010.03.010
25. Leitner H, Schnitzer R, Schober M, Zinner S. Precipitate modification in PH13-8 Mo type maraging steel. *Acta Mater.* **2011**, *59*, 5012–5022. DOI:10.1016/j.actamat.2011.04.053
26. Staron P, Jamnig B, Leitner H, Ebner R, Clemens H. Small-angle neutron scattering analysis of the precipitation behaviour in a maraging steel. *J. Appl. Crystallogr.* **2003**, *36*, 415–419. DOI:10.1107/S0021889803000293
27. Jamnig B, Ebner R, Staron P, Clemens H, Leitner H, Jeglitsch F, et al. On the Precipitation Behaviour in Maraging Steels. In Proceedings of the 6th International Tooling Conference, Karlstad, Sweden, 10–13 September 2002.
28. Guo Z, Sha W. Comments on *Small-angle neutron scattering analysis of the precipitation behaviour in a maraging steel* by Staron, Jamnig, Leitner, Ebner & Clemens (2003). *J. Appl. Crystallogr.* **2004**, *37*, 325–326. DOI:10.1107/S0021889803028127
29. Leitner H, Schober M, Schnitzer R, Zinner S. Strengthening behavior of Fe–Cr–Ni–Al–(Ti) maraging steels. *Mater. Sci. Eng. A* **2011**, *528*, 5264–5270. DOI:10.1016/j.msea.2011.03.058
30. Chen Y, Dai X, Chen X, Yang B. The characterization of G-phase in Fe20Cr9Ni cast duplex stainless steel. *Mater. Charact.* **2019**, *149*, 74–81. DOI:10.1016/j.matchar.2019.01.012
31. Hamaoka T, Nomoto A, Nishida K, Dohi K, Soneda N. Accurate determination of the number density of G-phase precipitates in thermally aged duplex stainless steel. *Philos. Mag.* **2012**, *92*, 2716–2732. DOI:10.1080/14786435.2012.674222
32. Hamaoka T, Nomoto A, Nishida K, Dohi K, Soneda N. Effects of aging temperature on G-phase precipitation and ferrite-phase decomposition in duplex stainless steel. *Philos. Mag.* **2012**, *92*, 4354–4375. DOI:10.1080/14786435.2012.707340
33. Pareige C, Novy S, Saillet S, Pareige P. Study of phase transformation and mechanical properties evolution of duplex stainless steels after long term thermal ageing (>20 years). *J. Nucl. Mater.* **2011**, *411*, 90–96. DOI:10.1016/j.jnucmat.2011.01.036

34. Li S, Wang Y, Wang X, Xue F. G-phase precipitation in duplex stainless steels after long-term thermal aging: A high-resolution transmission electron microscopy study. *J. Nucl. Mater.* **2014**, *452*, 382–388. DOI:10.1016/j.jnucmat.2014.05.069
35. Badyka R, Monnet G, Saillet S, Domain C, Pareige C. Quantification of hardening contribution of G-Phase precipitation and spinodal decomposition in aged duplex stainless steel: APT analysis and micro-hardness measurements. *J. Nucl. Mater.* **2019**, *514*, 266–275. DOI:10.1016/j.jnucmat.2018.12.002
36. Guo W, Garfinkel DA, Tucker JD, Haley D, Young GA, Poplawsky JD. An atom probe perspective on phase separation and precipitation in duplex stainless steels. *Nanotechnology* **2016**, *27*, 254004. DOI:10.1088/0957-4484/27/25/254004
37. Garfinkel DA, Poplawsky JD, Guo W, Young GA, Tucker JD. Phase Separation in Lean-Grade Duplex Stainless Steel 2101. *JOM* **2015**, *67*, 2216–2222. DOI:10.1007/s11837-015-1581-7
38. Pareige C, Emo J, Saillet S, Domain C, Pareige P. Kinetics of G-phase precipitation and spinodal decomposition in very long aged ferrite of a Mo-free duplex stainless steel. *J. Nucl. Mater.* **2015**, *465*, 383–389. DOI:10.1016/j.jnucmat.2015.06.017
39. Zhang B, Xue F, Li SL, Wang XT, Liang NN, Zhao YH, et al. Non-uniform phase separation in ferrite of a duplex stainless steel. *Acta Mater.* **2017**, *140*, 388–397. DOI:10.1016/j.actamat.2017.08.044
40. Yuan Y, Xie Y, Hou Z, Jin Q, Ke Y, Dong Z, et al. Synergistic effect of dislocation and elemental clustering on spinodal decomposition in super duplex stainless steel. *Mater. Charact.* **2025**, *221*, 114719. DOI:10.1016/j.matchar.2025.114719
41. Chen Y, Yang B, Zhou Y, Wu Y, Zhu H. Evaluation of pitting corrosion in duplex stainless steel Fe20Cr9Ni for nuclear power application. *Acta Mater.* **2020**, *197*, 172–183. DOI:10.1016/j.actamat.2020.07.046
42. Xia Z, Liu W, Li Y, Liu B, Qiu W, Xiong Y, et al. Effect of G-phase and heterogeneous deformation-induced strengthening on the mechanical properties of Cu-20Ni-20Mn-2Fe-1Si alloy. *Mater. Charact.* **2023**, *205*, 113325. DOI:10.1016/j.matchar.2023.113325
43. Dong H, Zhong R, Liu L, Wang Z, Yang C, Luo Z, et al. The intergranular precipitation behavior of G phase in a high-performance complex cast Cu-Ni-Al alloy. *Mater. Charact.* **2023**, *196*, 112611. DOI:10.1016/j.matchar.2022.112611
44. Jeong HW, Shin JY, Kwon SH, Kato H, Choi EA, Han SZ. Silicon effects on the formation of heterogeneous intermetallic compound phases in Cu-Ni-Si(-Mn) alloys under homogenization treatment. *Intermetallics* **2025**, *185*, 108913. DOI:10.1016/j.intermet.2025.108913
45. Zhang X, Li S, Liu Q, Zhao D, Zhang X, Wu P, et al. The effect of Sr on the microstructure and properties of Ni-Ti-Si type G-phase reinforced copper alloy. *Intermetallics* **2026**, *192*, 109245. DOI:10.1016/j.intermet.2026.109245
46. Zhang X, Liu Q, Zhao D, Liu Y, Hua S, Ding H. Growth and evolution of Ni-Ti-Si type G phase $Ni_{16}Ti_6Si_7$ in Cu alloys. *Mater. Charact.* **2024**, *216*, 114304. DOI:10.1016/j.matchar.2024.114304
47. Yang M, Wang C, Yang S, Shi Z, Liu X. New insights into the precipitation strengthening of ferritic steels: Nanoscale G-phase particle. *Mater. Lett.* **2017**, *209*, 134–137. DOI:10.1016/j.matlet.2017.07.078
48. Yang M, Zhu J, Wu C, Yang S, Shi Z, Wang C, et al. Microstructural evolution and precipitation strengthening in a new 20Cr ferritic trial steel. *Mater. Sci. Eng. A* **2019**, *742*, 734–742. DOI:10.1016/j.msea.2018.05.027
49. Yang M, Zhu J, Yang T, Luan J, Jiao Z, Fan X, et al. A novel ferritic steel family hardened by intermetallic compound G-phase. *Mater. Sci. Eng. A* **2019**, *745*, 390–399. DOI:10.1016/j.msea.2018.11.148
50. Yang M, King DJM, Povstugar I, Wen Y, Luan J, Kuhn B, et al. Precipitation behavior in G-phase strengthened ferritic stainless steels. *Acta Mater.* **2021**, *205*, 116542. DOI:10.1016/j.actamat.2020.116542
51. Yang M. Alloy Design, Aging Behavior and Mechanical Properties of the G-Phase Strengthened Fe-Ni-Si-Based BCC Structural Steels. Ph.D. Thesis, Xiamen University, Xiamen, China, 2019.
52. Wang CP, Hu Y, Yang SY, Lu Y, Jiang QW, Liu XJ. Experimental Investigation of Phase Equilibria in the Fe-Si-Zr Ternary System. *J. Phase Equilib. Diffus.* **2013**, *34*, 277–288. DOI:10.1007/s11669-013-0242-1
53. Hu X, Chen G, Ion C, Ni K. The 1100 °C isothermal section of the Ti-Ni-Si ternary system. *J. Phase Equilibria* **1999**, *20*, 508–514. DOI:10.1361/105497199770340761
54. Wang C, Huang X, Huang L, Yang M, Yang P, Cui Y, et al. Experimental Investigation of Phase Equilibria in the Co-Ta-Si Ternary System. *Materials* **2022**, *15*, 3097. DOI:10.3390/ma15093097
55. Wang C, Huang X, Yang M, Han J, Yao Z, Yang T, et al. Development of novel ferritic steels strengthened by the Co16X6Si7-G phase: A theoretical and experimental study. *Mater. Des.* **2022**, *222*, 111021. DOI:10.1016/j.matdes.2022.111021
56. King DJM, Yang M, Whiting TM, Liu X, Wenman MR. G-phase strengthened iron alloys by design. *Acta Mater.* **2020**, *183*, 350–361. DOI:10.1016/j.actamat.2019.11.007
57. Beattie HJ, Versnyder FL. A New Complex Phase in a High-Temperature Alloy. *Nature* **1956**, *178*, 208–209. DOI:10.1038/178208b0

58. Yang M, Huang C, Han J, Wu H, Zhao Y, Yang T, et al. Development of the high-strength ductile ferritic alloys via regulating the intragranular and grain boundary precipitation of G-phase. *J. Mater. Sci. Technol.* **2023**, *136*, 180–199. DOI:10.1016/j.jmst.2022.07.029
59. Bochenek K, Rogal Ł, Jarząbek D, Włoczewski M, Rygier T, Jenczyk P, et al. Rhenium-induced strengthening and microstructural stability in hot-pressed AlCoCrFeNi dual-phase high-entropy alloy. *Arch. Civ. Mech. Eng.* **2026**, *26*, 115. DOI:10.1007/s43452-026-01499-1
60. Turnali A, Hariharan A, Polatidis E, Peter NJ, Gehlmann J, Sofras C, et al. Harnessing additive manufacturing-induced microstructure and solute heterogeneities for the design of precipitation-strengthened alloys. *Acta Mater.* **2025**, *298*, 121423. DOI:10.1016/j.actamat.2025.121423
61. Ma K, Ferreirós PA, Pfeifer TW, Abernethy RG, von Tiedemann S, Peng N, et al. Intermetallic dispersion-strengthened ferritic superalloys with exceptional resistance to radiation-induced hardening. *Acta Mater.* **2025**, *293*, 121095. DOI:10.1016/j.actamat.2025.121095
62. Shen Z, Qiu N, Zhao L, Liang Z, Zuo X. Effects of Co-precipitation on local stacking fault energy modulation and Strength–Ductility synergy in Fe–Mn–Ni–Al–Cu–V–C austenitic steels. *Mater. Sci. Eng. A* **2026**, *950*, 149515. DOI:10.1016/j.msea.2025.149515
63. Liu Y, Pang X, He S, Zhang L, Lin Z, Du P, et al. In-situ formation of AlN nanoparticles in NiAl-strengthened ferritic alloy with enhanced high-temperature mechanical properties via SLM fabrication. *Mater. Sci. Eng. A* **2024**, *899*, 146460. DOI:10.1016/j.msea.2024.146460
64. Jiao ZB, Luan JH, Miller MK, Yu CY, Liu CT. Effects of Mn partitioning on nanoscale precipitation and mechanical properties of ferritic steels strengthened by NiAl nanoparticles. *Acta Mater.* **2015**, *84*, 283–291. DOI:10.1016/j.actamat.2014.10.065
65. Włoczewski M, Jasiewicz K, Jenczyk P, Gadalińska E, Kulikowski K, Zhang Y, et al. AlCoCrFeNi$Ti_{0.2}$ High-Entropy Alloy Under Plasma Nitriding: Complex Microstructure Transformation, Mechanical and Tribological Enhancement. *Met. Mater. Trans. A* **2025**, *56*, 2040–2056. DOI:10.1007/s11661-025-07752-1